Article

Not peer-reviewed version

Reduced-Order Modeling (ROM) of a Segmented Plug Flow Reactor (PFR) for Hydrogen Separation for Integrated Gasification Combined Cycles (IGCC)

Osama A. Marzouk *

Posted Date: 26 March 2025

doi: 10.20944/preprints202503.1980.v1

Keywords: hydrogen; palladium; membrane; permeate; retentate; syngas; reduced-order model

 doi:10.20944/preprints202503.1980.v1

Article

Reduced-Order Modeling (ROM) of a Segmented Plug Flow Reactor (PFR) for Hydrogen Separation for Integrated Gasification Combined Cycles (IGCC)

Osama A. Marzouk

College of Engineering, University of Buraimi, Al Buraimi, Sultanate of Oman; osama.m@uob.edu.om

Abstract: A reduced-order model (ROM) procedure for a one-dimensional steady plug-flow reactor (PFR) is developed and used to investigate the performance of a membrane reactor (MR), or membrane module (MM), for hydrogen separation from syngas that may be produced in an integrated gasification combined cycle (IGCC). A feed syngas enters from one side into a retentate zone, while a sweep gas of nitrogen enters from the opposite side into a neighbor permeate zone. The two zones are separated by permeable palladium membrane surfaces that are selectively permeable to hydrogen. After analyzing the hydrogen permeation profile in a base case (300 °C uniform temperature, 40 atm absolute retentate pressure, and 20 atm absolute permeate pressure), the temperature of the module, the retentate-side pressure, and the permeate-side pressure were varied individually and their influence on the permeation performance is investigated. In all the simulation cases, fixed targets of 95% hydrogen recovery and 40% mole-fraction of hydrogen at the permeate exit are demanded. The module length is allowed to change in order to satisfy these targets. Other dependent permeation-performance variables that are investigated include the logarithmic mean pressure-square-root difference, the hydrogen apparent permeance, and the efficiency factor of the hydrogen permeation. Various linear and nonlinear regression models are proposed based on the obtained results. This work gives general insights into hydrogen permeation via palladium membranes in a hydrogen membrane reactor (HMR). For example, the temperature is the most effective factor to improve the permeation performance. Increasing the absolute retentate pressure from the base value of 40 atm to 120 atm results in a proportional gain in the permeated hydrogen mass flux, with about 0.05 kg/m^2.hr gained per 1 atm increase in the retentate pressure; while decreasing the absolute permeate pressure from the base value of 20 bar to 0.2 bar causes the hydrogen mass flux to increase exponentially from 1.15 kg/m^2.hr. to 5.11 kg/m^2.hr.

Keywords: hydrogen; palladium; membrane; permeate; retentate; syngas; reduced-order model

1. Introduction

Gasification is a thermochemical process in which a carbonaceous solid fuel (such as coal or biomass) is converted into a synthesis gas, which is known as "syngas" [1–3]. In other words, gasification is a partial oxidation (substoichiometric) process consisting of physical processes, such as pyrolysis; and chemical reactions, such as gasification using steam [4,5]. Syngas is a mixture of gases, primarily carbon monoxide (CO) and hydrogen (H_2), with possible additional impurities such as carbon dioxide (CO_2), methane (CH_4), water vapor (H_2O), and nitrogen (N_2) [6]. Syngas is also produced from natural gas or light crude oil fractions through steam reforming [7]. The molar ratio of molecular hydrogen (H_2) to carbon monoxide increases as the ratio of hydrogen atoms to carbon atoms in the feedstock increases. Thus, ideal steam reforming of one mole of carbon gives a molar ratio of H_2:CO equal to 1:1, given the reaction

$$\mathbf{C + H_2O \rightarrow H_2 + CO} \qquad (1)$$

 doi:10.20944/preprints202503.1980.v1

which has one mole of hydrogen and one mole of carbon monoxide as the products. On the other hand, the ideal steam reforming of one mole of methane (as an approximation for natural gas) gives a molar ratio of H_2:CO equal to 3:1, given the reaction

$$\mathbf{CH_4 + H_2O \rightarrow 3\,H_2 + CO} \qquad (2)$$

which has three moles of hydrogen and one mole of carbon monoxide as the products [8].

Syngas has multiple uses beyond being a gaseous fuel that can be used in gas turbines or boilers [9,10]. For example, syngas is also a feedstock for the production of methanol, ammonia, synthetic gasoline, and hydrogen [11,12]. Syngas-based hydrogen particularly is of special environmental importance, as it enables the production of electricity through fuel cells without harmful carbon dioxide emissions [13,14]. Syngas-based hydrogen also can be used as an alternative clean fuel in hydrogen vehicles [15], leading to reduced greenhouse gas (GHG) emissions in the transportation sector and thus mitigating global warming effects [16,17], and leading also to improving the air quality in the built environment [18,19] since the combustion of hydrogen does not lead to carbon dioxide or toxic products [20,21] (but undesired nitrogen oxides or NOx "NO and NO_2" are still possible due to the oxidizing air [22]). In the power sector, nitrogen-diluted syngas-based hydrogen can be used in hydrogen-fueled gas turbines, with no harmful carbon dioxide emissions [23,24]. This dilution allows for reducing the combustion temperatures, and thus reducing the NOx emissions [25]. A nitrogen-diluted hydrogen flame with a fuel mixture having a chemical composition of 60% nitrogen and 40% hydrogen (mole fractions) was experimentally studied, and it was shown that this nitrogen dilution is effective in adjusting the flame length [26]. Separating hydrogen from syngas increases the concentration of carbon dioxide in the remaining content [27], thereby facilitating the carbon capture process afterward [28,29], which is similar to how using pure oxygen (rather than air) as an oxidizer in oxy-fuel combustion [30–33] causes the combustion products to be rich in carbon dioxide and this makes its capture easier [34,35]. The impurity carbon dioxide can be captured from the syngas, preventing its release into the atmosphere [36,37]. The captured carbon dioxide may be stored underground, and it may be utilized commercially for achieving economic gains in a different applications [38–40]. This carbon capture scenario is classified as a pre-combustion capture because carbon dioxide is segregated from the fuel stream (syngas in this case) before it is sent to the combustion facility [41,42].

Hydrogen separation from a hydrogen-containing gas mixture can be accomplished by various methods, including membrane separation [43,44]. Palladium-based (Pd-based) membranes allow the production of high-purity hydrogen [45–47], which is important for the effective operation of proton exchange membrane (PEM) fuel cells [48,49]. Palladium-based membranes are known for selectively separating hydrogen from a gas stream [50], which undergoes a dehydrogenation process as hydrogen is removed and is made to pass across the membrane. Compared to pressure swing adsorption (PSA), where adsorbing the impurities is used for hydrogen separation; membrane-based hydrogen separation allows for higher hydrogen recovery [51]. The term 'hydrogen recovery' means the fraction of hydrogen mass in a gaseous mixture that is extracted from that mixture. Thus, if all the hydrogen content in a mixture of gases is extracted, the hydrogen recovery reaches its highest value of 100% or 1.0. Pressure swing adsorption is a process used for separating a gas (such as hydrogen) from a mixture of gases, which is the same purpose as the palladium membrane in the current study, although the mechanism is very different. In PSA, selective adsorption-desorption takes place. When PSA is used in separating or purifying hydrogen, a mixture of gases containing hydrogen is pressurized, and then it passes through a reactor with an adsorbent material in the form of solid particles, which selectively attract the molecules of the impurities (the gases other than hydrogen) from the mixture onto their surface, as an adsorption stage, leaving hydrogen atoms at a high level of purity. Then, the pressure is decreased, which causes bound molecules of the impurities (the adsorbed non-hydrogen gases) to be released from the adsorbent surface, as a desorption stage [52]. Compared to cryogenic distillation, where impurities are condensed at low temperatures for purifying hydrogen; membrane purification is less energy intensive [53]. Cryogenic separation of hydrogen uses a refrigeration system to cool a gaseous mixture containing hydrogen [54]. Because

 doi:10.20944/preprints202503.1980.v1

the constituent gases of the mixture typically condense and change from a gaseous state into a liquid state at different temperatures (at different boiling points), non-hydrogen gases in the mixture condense first, leaving the hydrogen gas alone. Among all elements, hydrogen has the second lowest boiling point, which is about 20.3 K at a normal atmospheric pressure [55,56]; while helium has the lowest one, which is about 4.2 K at a normal atmospheric pressure [57,58]. Membrane-based hydrogen purification here refers to a pressure-driven process, where the selective permeation of hydrogen through the palladium membrane is stimulated by a difference in the partial pressure of hydrogen as it is transferred from the retentate side (before the hydrogen separation, where hydrogen has a higher partial pressure) to the permeate side (after the hydrogen separation, where hydrogen has a lower partial pressure). It may be worth mentioning that the carbon capture process (such as pre-combustion capture as demonstrated in the current study, or post-combustion-carbon capture and oxy-fuel carbon capture) is a retrofitting action to mitigate carbon dioxide (CO_2) emissions from existing energy systems or other industrial facilities [59,60]. For better environmental aspects, a total switch to renewable energy sources (particularly solar energy and wind energy [61]) is preferred because, in such scenarios, no carbon dioxide is produced [62–64]. However, such an energy transition toward renewable and sustainable resources may not be readily easy for existing conventional energy plants, whereas carbon capture strategies may remain suitable solutions for low-emission energy and process systems [65].

This work considers hypothetical membranes that are unsupported (bulk), relatively-thick, dense (non-porous) palladium foils for hydrogen separation. Catalytic reactors with dense metallic membranes for hydrogen production have shown a potential to overcome limitations on the yield that are associated with chemical equilibrium [66]. The mechanism of permeation through the membrane involves the dissociation of molecular hydrogen at the surface of the palladium membrane as hydrogen atoms, which then diffuse into the palladium membrane [67]. An isothermal hydrogen separation module (thus, having a uniform temperature) is adopted here. The spatial variation of the chemical composition of the permeate stream and retentate stream is modeled numerically as a plug-flow reactor. The permeation performance is examined under a reference set of representative conditions, as well as when each of the three control (design) variables is changed from the reference (base) case. These control variables are: (1) the reactor temperature, (2) the retentate-side pressure, and (3) the permeate-side pressure. Our study is based on simplified system-level computational modeling using principles of membrane-based hydrogen permeation. The interested reader can find some information about modeling a continuous plug-flow reactor in Appendix A.

The contributions of this work include: (1) the detailed step-by-step numerical model algorithm for membrane-based hydrogen permeation, (2) the regression models that qualitatively show the impact of three operational conditions on membrane-based hydrogen permeation, and (3) contrasting profiles of hydrogen recovery and mole fractions in an isothermal membrane reactor at a base case and three other extreme cases.

In the next section, the research method is described. Then, details about the geometric and inlet parameters are provided. Most of these settings remain fixed throughout the entire study. Then, the modeling procedure is described for the hydrogen permeation in the reactor. After this, five quantitative scalar quantities are introduced as criteria for evaluating the overall permeation performance. This is followed by a presentation of results for a base case, combined with a discretization-sensitivity analysis that confirms the adequacy of the spatial resolution utilized. Then, the influence of three control variables is explored, with some regression models relating the value of each control variable (as an independent or explanatory variable) to the five permeation metrics of the hydrogen permeation (as dependent or response variables). Finally, concluding remarks are provided.

2. Research Method

 doi:10.20944/preprints202503.1980.v1

The research conducted here is computational in principle, and it relies on the modeling of hypothetical units for the permeation of hydrogen from a feedstock (feed) gas stream to a destination stream called permeate.

2.1. Connection to Real-Life Application

The feed stream is representative of a realistic syngas flow in an integrated gasification combined cycle (IGCC), in which coal is converted into syngas [68–70]. This syngas drives gas turbines as the first source of power generation, and the heat content in the exhaust gases is partially recovered to produce steam as a working fluid for steam turbines, serving as the second source of power generation [71]. An IGCC power plant has an efficiency (with respect to the lower heating value, LHV) of about 48%, which means it has a higher efficiency (10-15% increase) and lower harmful emissions (10-15% reduction) compared to a conventional steam power plant operating by burning coal as a fuel [72–75].

2.2. Computer Modeling Tool

We perform the computational modeling through spreadsheets (Microsoft Excel software program), where the mathematical equations governing the hydrogen permeation along the membrane length are implemented as dependent formulas. The built-in tool "Goal Seek" within the Microsoft Excel desktop application (under the Microsoft Windows operating system) was utilized for solving the nonlinear algebraic equation relating the unknown membrane length to the specified hydrogen recovery target (95%) [76,77]. Obtaining a solution using this nonlinear solver tool is nearly immediate on a personal computer. This is a big advantage compared to multi-dimensional detailed computational fluid dynamics (CFD) models, which not only take more time and require more computing power, but also require advanced skills and specialized software for setting the model and running a computer solver [78–84]. While such detailed CFD models allow for more realistic solutions (such as three-dimensional flow fields), for a preliminary design stage, a quick and convenient tool may be advantageous for exploring the approximated impact of quantities of interest, particularly when only system-level operational parameters are desired; and such reduced-order modeling allows for rapid preliminary design, benchmarking, optimization and control, and parametric sensitivity analysis, and investigating the validity of wide ranges of operating conditions [85–88].

2.3. Controllable Variables

The variables that are subject to change in this work as independent parameters are: (1) the temperature of the membrane reactor (while keeping the retentate-side pressure and the permeate-side pressure at reference values of a base case), (2) the retentate-side pressure (while keeping the temperature and the permeate-side pressure at reference values of a base case), and (3) the permeate-side pressure (while keeping the temperature and the retentate-side pressure at reference values of a base case).

For each of the three scenarios listed above, the influence of the isolated design variable on the hydrogen permeation and fluid flow is investigated.

2.4. Some Assumptions

Some assumptions are made in the present work, which reduces the interaction of factors and makes the interpretation of cause-effect dependence more evident. Such assumptions include the uniformity of the temperature, and ignoring the effect of permeation on the pressures [89]. It is acknowledged that these assumptions limit the generality of the results. However, the study focuses on trends and patterns of relational dependence between variables for a simplified configuration. Thus, the results presented here can be useful when regarded as broad guides rather than universal facts. The assumption of constant temperature (isothermal environment) seems proper since the

 doi:10.20944/preprints202503.1980.v1

modeled dehydrogenation process does not involve internal heat sources, combustion, coolants, or external heat exchange [90].

The detailed steps of the numerical modeling procedure for the proposed palladium-based hydrogen separation are presented in Appendix B.

2.5. Flow Setup

Figure 1 is a sketch of the stream directions and the compositions of the feed (inlet of the retentate side, in the shell) and the sweep (inlet of the permeate side, inside the tubes). Instead of showing all eight tubes (which can make the sketch unclear), only the central tube is shown. The coordinate (x) is the longitudinal distance measured from the left edge of the membrane reactor. The feed syngas enters the shell from the left, and the sweep nitrogen enters the tubes from the right.

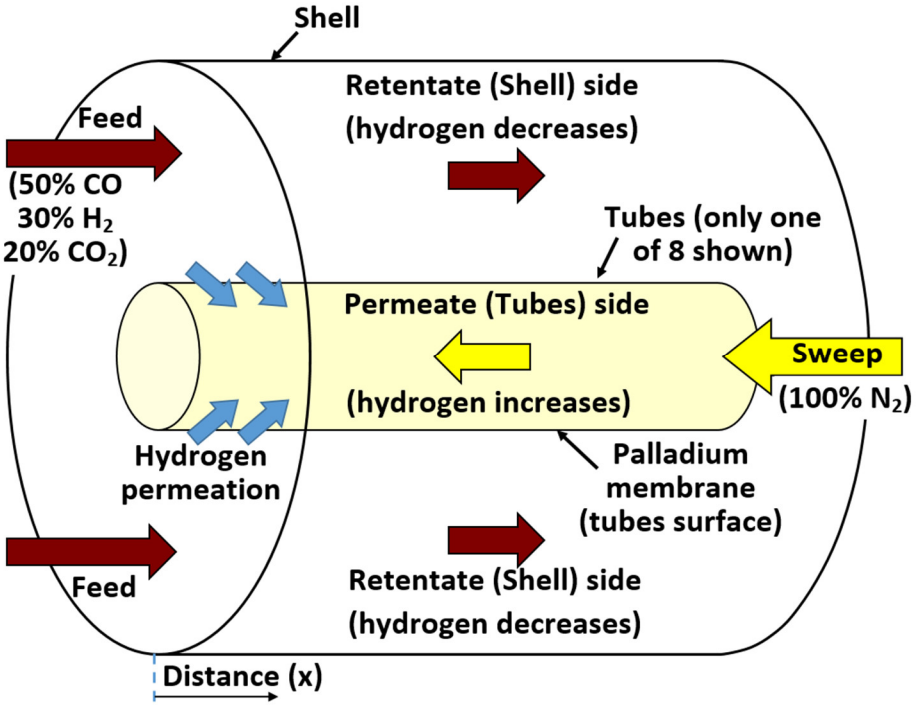

Figure 1. Inlet conditions and flow directions for retentate and permeate streams.

The counter-flow profile used here for the streams (where the two streams enter from the opposite ends of the membrane reactor) is preferred over the parallel or co-flow profile (when the two streams enter the membrane reactor from the same edge and exit from the same edge). This is due to a more even distribution of the driving force for the mass transfer of hydrogen from the retentate side to the permeate side. This advantage of counter-flow design over parallel flow (co-flow) design exists also in the field of heat exchangers, where heat transfer rather than mass transfer is sought [91–93].

3. General Model Settings

3.1. Fixing Common Parameters

This section illustrates various elements of the hydrogen separation modeling that remain unchanged for all simulation cases. They may be classified into two groups: (1) geometric parameters, and (2) flow parameters. It should be noted that this work is not primarily intended to solve a particular problem or recommend a specific design. Instead, more value is provided by examining variations of permeation parameters when three operational variables are changed. Thus, any

 doi:10.20944/preprints202503.1980.v1

reasonable selection of settings is considered satisfactory here to establish a starting design point in the design space.

3.2. Underlying Geometry

All the imagined hydrogen separation modules investigated in this study share the same presumed geometric configuration except for the length. Such a proposed module is in the form of a shell-and-tube reactor, with eight cylindrical tubes placed inside a cylindrical shell. The sum of the cross-sectional areas of the tubes is 50% of the cross-sectional area of the outer enclosing cylinder, which forms the outer boundary of the shell. In the current work, the term "shell" means the part of the outer enclosing cylinder that remains after subtracting the tubes. Thus, it refers to the passage available for the gaseous stream to flow around the tubes but within the outer enclosing cylinder. This stream is referred to as the shell stream or the retentate. It is the fluid stream where the syngas feedstock enters and loses hydrogen during a dehydrogenation process to the other stream located inside the tubes. The retentate stream entering the shell is referred to as the feed, which means the raw syngas that is supplied before any processing by the hydrogen permeation membranes.

The other stream located inside the eight tubes is the tube-side stream or the permeate. It is the destination of the hydrogen that is transported from the retentate through the palladium membranes. At the inlet of the permeate, a non-hydrogen gas of molecular nitrogen (N_2) is supplied in the current model. This intentionally added nitrogen is referred to as the sweep gas or the sweep. While the use of such sweep gas is, strictly speaking, optional, it helps improve the permeation process by ensuring that the permeate side can never be saturated with hydrogen, and it increases the difference in the hydrogen partial pressures across the membrane, leading to an increased hydrogen permeation flux [94–97]. The added sweep gas can play another function of controlling the temperature [98], but this is not considered here as we assume the membrane reactor to be isothermal for simplicity. Other gases can also be used as a sweep gas, such as argon, Ar [99–102]; steam, H_2O [103–106]; helium, He [107–110]; or a mixture of gases [111–116]. The use of nitrogen here seems adequate [117,118].

The shell-and-tube reactor configuration was used in another study [119] while computationally modeling the propane steam reforming process under high temperatures (between 750 K and 900 K). In the propane steam reforming process, propane (C_3H_8) reacts with steam (H_2O) to produce molecular hydrogen (H_2) and carbon dioxide (CO_2). This reformation reaction takes place within a porous medium acting as a catalyst. Unlike the present study, the model in that external study did not include hydrogen separation. The tubes in the reactor were used in that external study to heat the surrounding porous shell through passing hot gases.

Another computational study for propane steam reforming (as a method for producing hydrogen from propane) used the shell-and-tube configuration [120–123]. There is a difference between the modeled reactor in that study and the modeled reactor in the present work. The reactor in the external study was a reformer with a catalytic chemical reaction taking place inside it, while here it is a separator with selective permeance (selective mass transport) but without a chemical reaction between gaseous species. However, there are some similarities between the two studies. One similarity is that both modeling methods assumed a steady flow (no change with time). Also, the flow entering the tubes (heating gas) and the flow entering the shell (reactant propane and steam) in the other study flow in opposite directions longitudinally, which is the same situation here for the retentate stream and the permeating stream.

Outside the field of hydrogen generation or separation (purification), shell-and-tube reactors can be used for heat transfer processes, when the fluid in the tubes is used to heat or change the phase of the fluid in the shell (or vice versa) without direct contact. The heat transfer performance can be improved by adding baffles of different geometries that alter the path of the fluid in the shell and control its level of mixing through intensified turbulence [124–126]. The shell-and-tube configuration is also viable in multiphase flows [127,128].

 doi:10.20944/preprints202503.1980.v1

In other research work, a palladium-based membrane reactor of steam methane reforming (MR-SMR) was optimized with two objectives which are (1) minimum heat exchange, and (2) minimum power consumption – through reducing the pressure gradient that should be counteracted by an external compressor unit [129,130]. In that reported work, by controlling the exterior wall temperature, it was found possible to achieve a saving of 5.1% for the power consumption and a drop of 1.4% for the rate of heat exchange. The membrane reactor was tubular (a single tube inside a single tube). It was treated as a plug flow reactor, given the high aspect ratio (large length compared to the diameter). The outer annular tube is the reaction zone (where methane reacts with steam to produce hydrogen), while the inner circular tube is the permeation zone (hydrogen permeates from the outer tube to the inner tube through a separating palladium membrane). The outer annular tube has a catalyst in the form of particles uniformly filling the outer annular tube, making it a porous 'packed bed'. The palladium membrane was dense.

Figure 2 shows a proposed cross-section of the membrane reactor, indicating the areas of the eight tubes (yellow color) and the area of the shell (white color). To obtain more uniform gaps between walls, one of the tubes is placed exactly at the center of the shell. The remaining seven tubes are arranged with equal circumferential spacing. It should be mentioned that the plug-flow reactor modeling conducted here utilizes the details about the layout of tubes when calculating the total perimeter of the palladium membranes (but the shell outer diameter is not utilized in the permeation calculation). In addition, such a layout provides justification for the adopted membrane perimeter, and also helps the reader envision how the membrane reactor looks in a real situation.

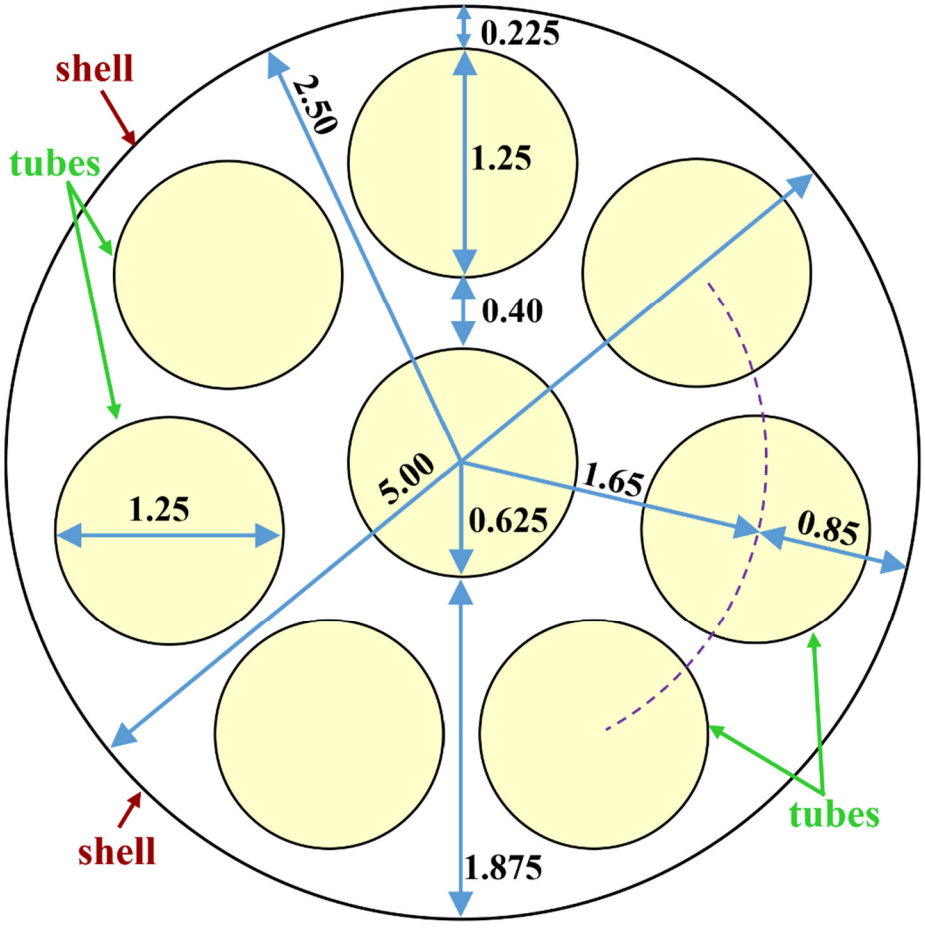

Figure 2. Proposed cross-section of the shell-and-tube membrane reactor (all dimensions are in cm).

Table 1 shows some details about the shell-and-tube geometry. The tubes and shell are assumed to have zero thickness, and the palladium membranes cover the entire surface of each tube. Being a reduced-order one-dimensional model, there are no baffles in the membrane reactor [131–133].

 doi:10.20944/preprints202503.1980.v1

Table 1. Some fixed geometric details about the proposed shell-and-tube membrane reactor.

Geometric feature	Value
Shell diameter	5.000 cm (1.969 in)
Tube diameter	1.250 cm (0.4921 in)
Number of tubes	8
Shell cross-section area (excluding tubes)	9.817 cm^2 (1.522 in^2)
Tubes cross-section area (all 8 tubes)	9.817 cm^2 (1.522 in^2)
Shell-to-tubes area ratio	1: 1
Tube cross-section area (single tube)	1.227 cm^2 (0.1902 in^2)

3.3. Fixed Conditions

Table 2 shows some details about the retentate stream, whose inlet conditions correspond to the raw syngas (the feed) supplied to the membrane reactor. The temperature and pressure are considered uniform in that stream. The temperature and pressure values are not specified because they are not common in all simulation cases, but are varied and their influences later are studied in multiple simulations.

Table 2. Some common fixed properties of the retentate stream.

Condition	Value
Inlet mole fraction, H_2	30% [134]
Inlet mole fraction, CO	50% [135]
Inlet mole fraction, CO_2	20% [136,137]
Molecular weight, H_2	2.01588 kg/kmol [138]
Molecular weight, CO	28.0101 kg/kmol [139]
Molecular weight, CO_2	44.0095 kg/kmol [140]
Molecular weight, mixture	23.412 kg/kmol
Inlet mass fraction, H_2	0.025832
Inlet mass fraction, CO	0.598207
Inlet mass fraction, CO_2	0.375961
Inlet mass flow rate	60 kg/hr (132.28 lbm/hr)
Inlet standard volume flow rate	970,068 sccm (standard cubic centimeters per minute)
Target hydrogen recovery	95% (by mass, by mole, or by standard volume - identical)

The mixture molecular weight of the feed (MW_{mix}) is calculated from the mole fractions and molecular weights of the constituent gases as follows [141,142]:

$$\mathbf{MW}_{mix} = \mathbf{MW}_{\mathbf{H2}}\, X_{H2} + \mathbf{MW}_{\mathbf{CO}}\, X_{CO} + \mathbf{MW}_{\mathbf{CO2}}\, X_{CO2} \qquad (3)$$

where (MW) refers to the molecular weight, (X) refers to the mole fraction, and the subscripts refer to the individual gases.

The mass fraction (Y) for each constituent gas in the feed is dependent upon its mole fraction (X) according to [143]

$$Y_i = \frac{\mathbf{MW_i}\, X_i}{MW_{mix}} \qquad (4)$$

where the subscript (i) refers to any gas of the constituent gases in the feed.

 doi:10.20944/preprints202503.1980.v1

The standard volume flow rate is the virtual volume flow if the temperature and pressure are at standard values, which are taken here as T_{stnd} = 0 °C (32 °F, 273.15 K) and P_{stnd} (absolute pressure) = 10^5 Pa (0.9869 atm, 14.504 psi). These two standard values of temperature and pressure are based on the International Union of Pure and Applied Chemistry, IUPAC [144].

An ideal gas is a gas that obeys the ideal-gas equation of state, which can be expressed as

$$\boldsymbol{P\,V = N\,\bar{R}\,T} \quad (5)$$

where (P) is the pressure, (V) is the volume, (N) is the number of moles, ($\bar{R}$) is the universal gas constant, and (T) is the absolute temperature, expressed in kelvins. For an ideal gas, each mole occupies a volume of 22,711 cm^3 (22.711 liters) at the standard pressure and temperature mentioned earlier. Thus, the standard volume is directly proportional to the number of moles, which in turn (and assuming no change occurs in the chemical composition of the gas) is directly proportional to the mass. This value can be obtained from the ideal-gas equation of state by solving for the standard volume per mole (V_{stnd}/N) as:

$$\frac{V_{stnd}}{N} = \bar{R}\frac{T_{snd}}{P_{stnd}} = (10^6)\left(8.3145\,\frac{J}{mol.K}\right)\left(\frac{273.15\,K}{10^5\,Pa}\right) = 22,711\,\frac{cm^3}{mol} \quad (6)$$

where the multiplier (10^6) is inserted to convert the volume unit from cubic meters (m^3) to cubic centimeters (cm^3), and the value of the universal gas constant ($\bar{R}$) is a physical constant taken from the U.S. National Institute of Standards and Technology [145]. The shown value in the above equation is a truncated version of the published one used in the computation, which is 8.314462618 J/mol.K.

Table 3 shows some details about the permeate stream, whose inlet conditions correspond to the sweep gas supplied to the membrane reactor. The temperature and pressure are considered uniform in that stream.

Table 3. Some common fixed properties of the permeate stream.

Condition	Value
Inlet gas	100% N_2
Molecular weight, N_2	28.0134 kg/kmol [146]
Inlet mass flow rate	30.692 kg/hr (67.664 lbm/hr)
Inlet standard volume flow rate	414,704 sccm (standard cubic centimeters per minute)
Target outlet mole fraction of H_2	40%

The flow rate of the sweep gas is decided based on the target mole fraction of hydrogen in the permeate outlet ($X_{H2,per\text{-}out}$), the mass flow rate of hydrogen in the syngas ($\dot{m}_{H2,feed}$), and the target hydrogen recovery (β) according to:

$$\dot{m}_{sweep} = \frac{MW_{N2}\,(1-X_{H2,per-out})}{MW_{H2}\,X_{H2,per-out}}\,\beta\,\dot{m}_{H2,feed} \quad (7)$$

The above relation can be used under the condition that there is only nitrogen in the sweep gas (which is true in all the simulations in the present work). It is a special relation and should not be used in other configurations, such as when the sweep gas is a mixture.

In the present work, β = 0.95, $X_{H2,per\text{-}out}$ = 0.4, and $\dot{m}_{H2,feed}$ = 1.5499 kg/hr (this is the product of the feed mass flow: 60 kg/hr, and the mass fraction of hydrogen in the feed: 0.025832). With the previously mentioned molecular weights of hydrogen (Table 2) and nitrogen (Table 3), we get $\dot{m}_{sweep}$ = 30.692 kg/hr as mentioned in Table 3.

The mass flow rates (and the standard volume flow rates) and the chemical compositions of the sweep gas and the feed gas are fixed in all the simulations of this work.

 doi:10.20944/preprints202503.1980.v1

4. Hydrogen Permeation Metrics

After performing a complete steady-state simulation for the palladium membrane permeation of hydrogen in a segmented plug-flow reactor, assessment of the overall permeation process is facilitated using a number of quantitative scalar quantities (referred to here as performance metrics or permeation metrics), that are convenient to utilize for comparing the performance of different simulations. In this section, five performance metrics for hydrogen separation are discussed.

4.1. Membrane Length

The first permeation performance metric adopted here is the needed membrane length to achieve the target hydrogen recovery ($\beta = 95\%$). This is designated by the symbol (L).

A smaller membrane length is desired, because it means a shorter membrane reactor, which is a better design due to reduced cost and space.

4.2. Average Hydrogen Permeation Mass Flux

The second permeation performance metric adopted here is the average mass flux (mass flow rate per unit area) of the permeated hydrogen through the membrane. It is designated by the symbol ($\bar{M}_{H2}$). Since the local mass flux of the permeated hydrogen is subject to variation from one segment to another in the membrane reactor model, the average of all segmental values is used. This metric is related to the corrected (second-iteration) segment-level molar flux of permeating hydrogen through the palladium membrane ($J_{H2,i}$) as

$$\bar{M}_{H2} = 3.6\, MW_{H2} \frac{1}{n} \sum_{i=1}^{n} J_{H2,i} \quad (8)$$

where (MW_{H2} = 2.01588 kg/kmol) is the molecular weight of the molecular hydrogen, and the factor (3.6) appears to enable unit conversion such that the average mass flux is expressed in (kg/m^2.hr) when the segmental mole flux ($J_{H2,i}$) is expressed in (mol/m^2.s).

A higher average mass flux is desired, as it shows more intense utilization of the membrane surface (better use of each unit area).

In the present study, because the total permeated hydrogen is fixed (by fixing the inlet mass flow of hydrogen in the syngas feed and fixing the target hydrogen recovery), and the membrane perimeter is also fixed, then the average hydrogen mass flux ($\bar{M}_{H2}$) and the membrane length (L) are not independent. Instead, they are inversely proportional to each other, and their product should be invariant.

4.3. Log Mean Pressure-Square-Root Difference

The third permeation performance metric adopted here is a global (membrane-level, not a segment-level) pressure-square-root difference, which is a membrane-level difference of the hydrogen partial pressure raised to the power of 0.5, between the retentate stream (higher value) and the permeate stream (lower value). It is designated here by the symbol (LMPsrD), or simply (LMPD), and is called log (or logarithmic) mean pressure-square-root difference. This difference in the square root of the hydrogen partial pressure (PsrD) stimulates the permeation through the palladium membrane. Because this stimulus driving force can vary along the membrane segments, an average value is sought. Instead of a simple arithmetic average over all segments, a logarithm-based average is used, which takes into account the differences at the left end and at the right end of the entire membrane reactor (where the flow inlets and outlets are located). Unlike computing a simple average of the driving force (the difference in the square root of the hydrogen partial pressure, or PsrD) along the membrane, the LMPD is related to the change in this driving force between the two ends of the hydrogen separation modules only, and this makes this metric simpler to compute without the need to know the details of the driving force between the two side ends of the hydrogen separation module. This resembles an approach of calculating an overall temperature difference in the field of

 doi:10.20944/preprints202503.1980.v1

heat transfer within heat exchangers, which is called log mean temperature difference, or LMTD [147]. The global log mean pressure-square-root difference is calculated as follows:

$$\mathbf{LMPD} = \frac{\left(\Delta P_{H2}^{0.5}\right)_{LHS,1} - \left(\Delta P_{H2}^{0.5}\right)_{RHS,n}}{ln\left(\left(\Delta P_{H2}^{0.5}\right)_{LHS,1}\right) - ln\left(\left(\Delta P_{H2}^{0.5}\right)_{RHS,n}\right)} \qquad (9)$$

where $(\Delta P_{H2}{}^{0.5})_{LHS,1}$ is the driving force at the left end of the membrane reactor (at x = 0), $(\Delta P_{H2}{}^{0.5})_{RHS,n}$ is the driving force at the right end of the membrane reactor (at x = L), and the (ln) function is the natural logarithm. The LMPD should lie between $(\Delta P_{H2}{}^{0.5})_{LHS,1}$ and $(\Delta P_{H2}{}^{0.5})_{RHS,n}$, regardless of which of them is larger than the other.

A higher log mean pressure-square-root difference (LMPD) is desired, as it is an indicator of the average driving force for hydrogen permeation between the left end and the right end of the membrane reactor, and is interpreted in a similar way to the LMTD in heat exchanges, being the driving force for heat transfer [148].

4.4. Global Apparent Permeance

The fourth permeation performance metric adopted here is the global apparent permeance (k'_{app}), which is a solution-dependent variable that represents the effective permeance based on the obtained profile of hydrogen permeation in the membrane reactor. It has the same unit of the actual (ideal) permeance (k'), which is an input parameter that depends on the temperature and the membrane length, and thus can be computed prior to the numerical simulation of the plug-flow reactor. To explain the usefulness and significance of the global apparent permeance (k'_{app}), it should be noted that the actual permeance (k') is a local value, corresponding to a specific segment (or even a specific point), and it depends on the temperature and the membrane thickness, as in Equation (B.14). However, the apparent permeance is computed based on the overall performance of the membrane reactor as a whole, as follows:

$$\boldsymbol{k'_{app}} = \frac{\frac{1}{n}\sum_{i=1}^{n} J_{H2,i}}{\mathbf{LMPD}} \qquad (10)$$

Therefore, two dehydrogenation palladium membrane reactors may have the same actual permeance because they have the same uniform temperature and the same uniform thickness, but due to variations in the dehydrogenation performance, they can have different global apparent permeance values. This makes the global apparent permeance a good metric for assessing the dehydrogenation process.

The numerator in the above equation is the arithmetic average of the molar flux of permeating hydrogen through the palladium membrane (average of the n segmental values), while the denominator is the log mean pressure-square-root difference (LMPD).

A higher apparent permeance is desired, as it shows that the membrane reactor yields a higher useful output (hydrogen molar flux) for a given average input (hydrogen pressure driving force).

4.5. Efficiency Factor

The fifth and last permeation performance metric adopted here is the efficiency factor (η_k), which is simply the ratio of the global apparent permeance to the local actual permeance, expressed as a percentage. Therefore,

$$\boldsymbol{\eta_k} = \frac{\boldsymbol{k'_{app}}}{\boldsymbol{k'}} \qquad (11)$$

The efficiency factor is the only permeation metric presented here that is non-dimensional, which makes it unambiguous and identical in any system of units.

The "efficiency factor" is not strictly an efficiency as used in energy conversion by a heat engine [149], being an output useful energy that is a fraction of an input heat energy, thus limited to a ceiling value of 100% [150]. Instead, the "efficiency factor" is a ratio between two quantities that have the same dimensional units but have different meanings, and either of them is allowed to exceed the other. Thus, the "efficiency factor" used here can exceed 100%. This is somehow similar to the concept

 doi:10.20944/preprints202503.1980.v1

of Octane number or the Research Octane Number (RON) as quality scale for gasoline (petrol) automotive fuels, where this rating does not strictly to be bound by a limit of 100 [151,152].

A higher efficiency factor is desired, as it is directly proportional to the global apparent permeance, thus it is related to the goodness of the membrane reactor operation with regard to hydrogen permeation.

5. Results

5.1. Base Case and Spatial Resolution Test

The first implementation of the plug-flow membrane reactor model is referred to as the base case or reference simulation. To run a simulation, three thermodynamic properties that describe the two flowing streams in the reactor are needed. These three properties are: (1) temperature (assumed uniform in the entire reactor), (2) retentate pressure (assumed uniform in the retentate stream), and (3) permeate pressure (assumed uniform in the permeate stream).

The uniform-temperature assumption avoids ambiguity when computing the actual (ideal) permeance of the palladium membrane, which is temperature-dependent. Thus, the actual permeance is also uniform in the entire membrane, and this eliminates an undesirable distracting influence from varying permeance.

The three aforementioned thermodynamic properties are to be varied individually later, deviating from their base values. The influence of each of them on the hydrogen permeation is examined.

The base case is considered to have representative (realistic) values of the membrane streams [153–155], which are summarized in Table 4.

Table 4. Temperature and pressures of the base case (reference simulation).

Fluid property	Value
Temperature	300 °C (572.00 °F)
Absolute retentate pressure	40.0 atm (587.84 psia)
Absolute permeate pressure	20.0 atm (293.92 psia)

The local actual hydrogen permeance (k') for the base temperature of (300 °C, 573.15 K) is 10.263 × 10^{-4} mol/m^2.s.$Pa^{0.5}$.

Table 5 gives numerical results for the base case after a complete simulation of the segmented plug-flow reactor for it. The normal resolution of 200 segments is compared with another resolution with twice the number of segments (400 segments) having the same membrane length found necessary for the 200-segment case.

Table 5. Some results obtained for the base case with 200 segments (normal resolution) and 400 segments (refined resolution for testing only).

Result	Value		Absolute percentage change
	n = 200 segments	n = 400 segments	$\frac{\lvert Value(200) - Value(400)\rvert}{Value(200)}$
Membrane length (cm)	407.359	407.359	0% (identical)
Average hydrogen permeation mass flux (kg/m^2.hr)	1.151	1.150	0.01%

 doi:10.20944/preprints202503.1980.v1

Pressure-square-root difference at the left end ($Pa^{0.5}$)	202.345	202.345	0% (identical)
Pressure-square-root difference at the right end ($Pa^{0.5}$)	260.655	268.896	3.16%
Log mean pressure-square-root difference ($Pa^{0.5}$)	230.271	234.05	1.64%
Global apparent hydrogen permeance ($mol/m^2.s.Pa^{0.5}$)	6.8849×10^{-4}	6.7732×10^{-4}	1.62%
Efficiency factor (%)	67.09%	66.00%	1.62%
Hydrogen recovery (%)	95.000%	94.991%	0.01%

Also, the absolute percentage deviations of these results between the two resolutions are shown in the table. Such comparison reveals small deviations not exceeding 2% in all four permeation performance metrics other than the membrane length, which was forced to be identical in the two simulations. Namely, these metrics are: (1) average hydrogen permeation mass flux, (2) log mean pressure-square-root difference, (3) global apparent hydrogen permeance, and (4) efficiency factor.

For the hydrogen recovery, it was a specified input in the case of using 200 segments, where the membrane length was a computed output. In the case of using 400 segments, the membrane length was the specified input (to ensure geometric consistency between the two simulations), while the hydrogen recovery was computed from the segmented plug-flow reactor model, in an inverse simulation mode. There is an insignificant difference (0.01% absolute change) in the two values of the hydrogen recovery.

In addition to the demonstrated quantitative agreement between the normal-resolution simulation with 200 segments and the high-resolution validation simulation with 400 segments, the qualitative agreement can also be observed in Figure 3. This figure compares the cumulative hydrogen recovery along the base-case plug-flow reactor model, for the 200-segment resolution and the 400-segment resolution. The profiles under both resolutions are visually indistinguishable.

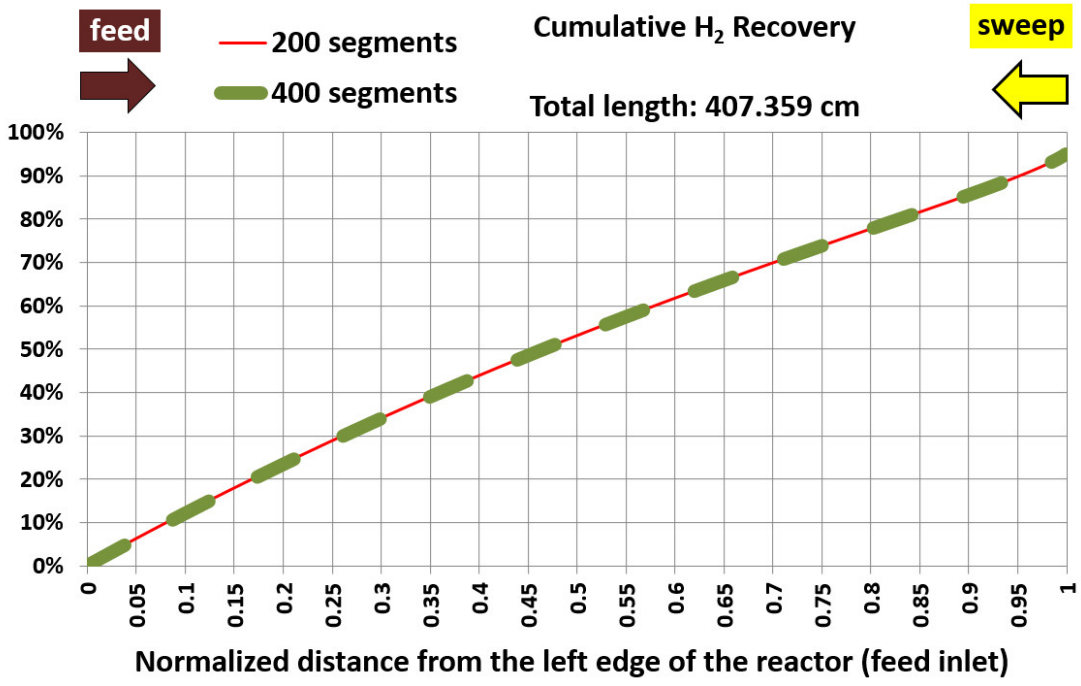

 doi:10.20944/preprints202503.1980.v1

Figure 3. Commutative hydrogen recovery for the base case, with two spatial resolutions (the 200 segments represent the normal resolution adopted in the study; the 400 segments represent the finer resolution for testing the resolution insensitivity).

Figure 4 shows the segmental hydrogen recovery profile (contribution of each reactor segment to the total hydrogen recovery). The normal resolution (200 segments) corresponds to nearly twice the values of the high resolution (400 segments). Although this may indicate a mismatch between the two simulations, it is actually appropriate because each segment under the normal resolution has twice the membrane area of a segment under the high resolution. For a meaningful visual comparison, a third curve was added to the figure by doubling the segmental hydrogen recovery obtained under high resolution (because each data point, in this case, represents only half of what a data point represents in the case of normal resolution). When the added curve (the adjusted high-resolution curve) is compared with the normal resolution curve, it is seen that both curves are visually identical.

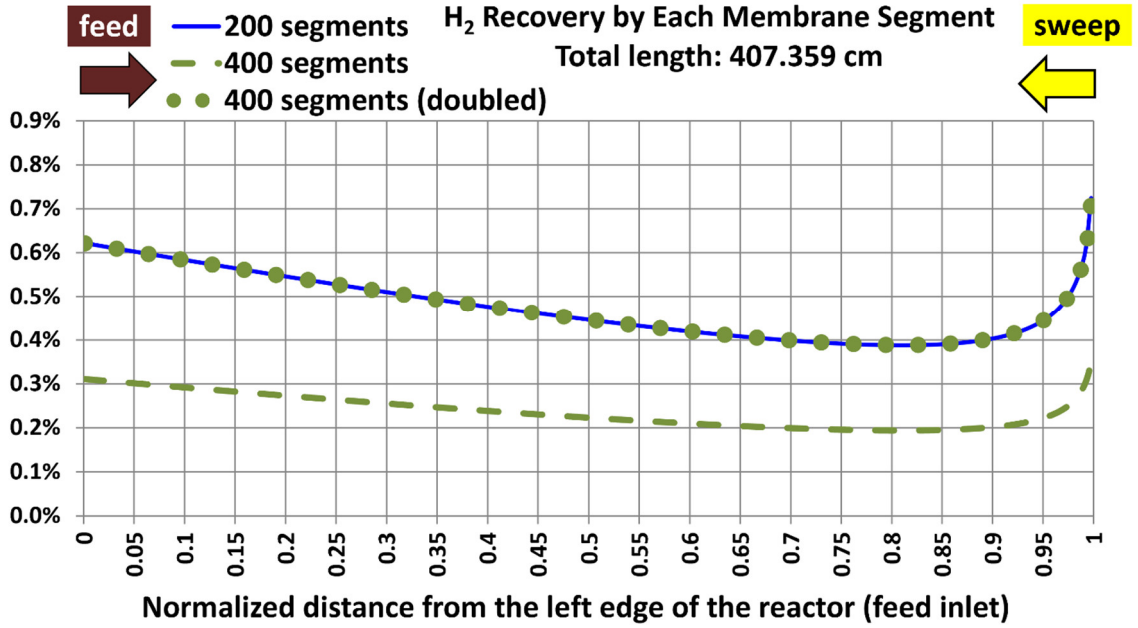

Figure 4. Segmental hydrogen recovery for the base case, with two spatial resolutions (the 200 segments represent the normal resolution). There is a third curve added, with the segmental recovery values in the case of 400 segments being doubled.

The nonlinear profile of the segmental recovery is attributed to the underlying variation in the driving force for the segmental hydrogen permeation (the segmental pressure-square-root difference), which is a nonlinear function of the hydrogen mole fraction in the permeate stream and the hydrogen mole fraction in the retentate stream.

The variations of the hydrogen mole fraction in the retentate stream as the retentate gas traverses the membrane reactor from the left to the right are shown in Figure 5. It decreases from 30% at the left end corresponding to x/L = 0 to 2.10% at the right end corresponding to x/L = 1. The variation is weekly nonlinear with the distance. The exit mole fraction is not exactly zero, but this is consistent with the target hydrogen recovery of 95%. The value of the exit mole fraction of hydrogen (2.10%) and the longitudinal pattern of that mole fraction for the normal resolution (200 segments) are consistent with those for the validation resolution (400 segments).

 doi:10.20944/preprints202503.1980.v1

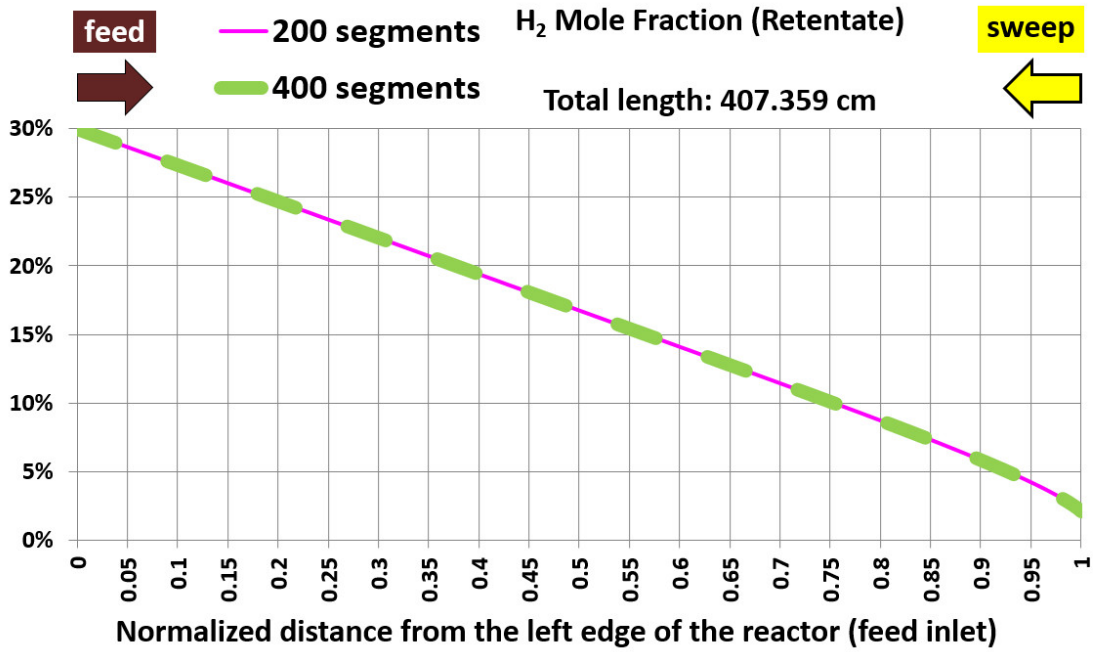

Figure 5. Hydrogen mole fraction in the retentate stream for the base case, with two spatial resolutions (the 200 segments represent the normal resolution).

The variations of the hydrogen mole fraction in the permeate stream as the permeate gas traverses the membrane reactor from the right to the left are shown in Figure 6. It increases from 0% at the right end corresponding to x = L (a normalized variable x/L = 1 is used in the figure) to the target 40% at the left end corresponding to x = 0. The variation is weekly nonlinear with the distance, as in the case of the retentate stream. Comparing the mole fraction patterns with 200 segments and with 400 segments suggests independence of the results on the spatial resolution. Thus, using 200 segments is adequate and there is no need to use a higher resolution.

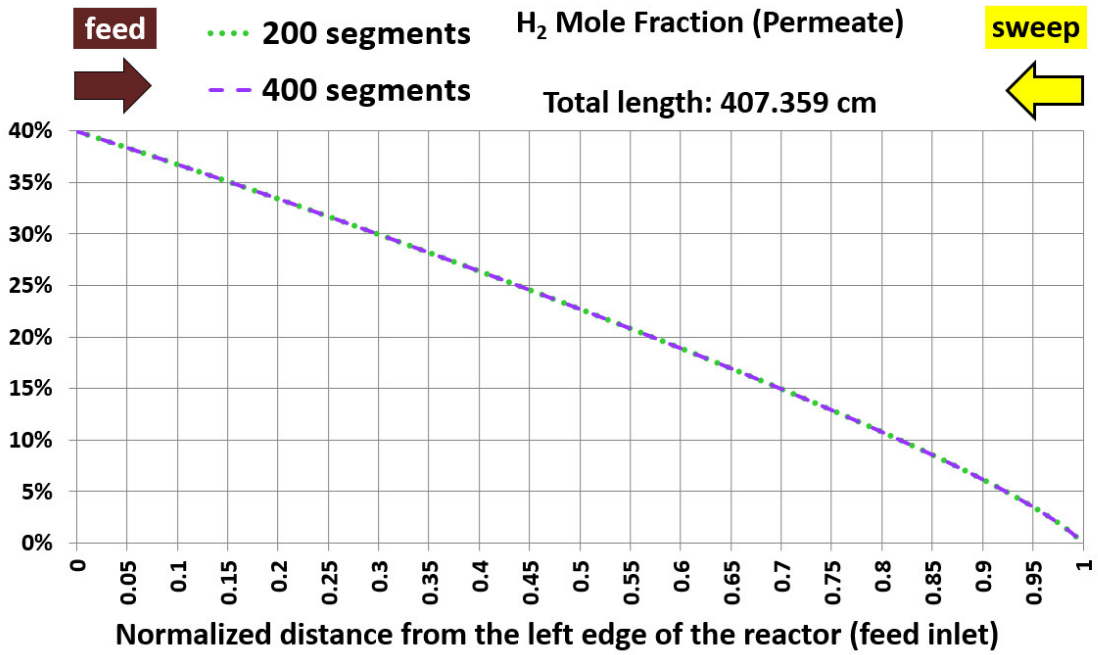

Figure 6. Hydrogen mole fraction in the permeate stream for the base case, with two spatial resolutions (the 200 segments represent the normal resolution).

 doi:10.20944/preprints202503.1980.v1

With such observed good agreement between the normal spatial resolutions and the testing high resolution, the choice of 200 segments (normal resolution) is considered satisfactory, and is adopted in all remaining simulations.

5.2. Influence of Temperature

After completing the segmented flow reactor under a set of representative operational conditions, the temperature of the flows in the membrane reactor is varied in a discrete manner, leading to a number of temperatures that are higher than the base value of 300 °C. The base value and the six additional temperatures are:

1. 300 °C (base)
2. 350 °C
3. 400 °C
4. 500 °C
5. 600 °C
6. 700 °C
7. 800 °C

It is understood that high temperatures may pose practical challenges for the materials and the process feasibility. Despite this, the model allows exploring the change in the permeation performance due to elevated temperatures. This is achieved by monitoring the changes in the five performance metrics due to the changes in the temperature alone. The other two design variables (retentate pressure and permeate pressure) are kept at their base values (40 atm absolute and 20 atm absolute, respectively).

Figure 7 shows the influence of the temperature on the first hydrogen permeation metric, which is the membrane length. The figure shows a monotonic nonlinear decline in the needed membrane length as the temperature increases. This dependence can be described by a nonlinear power-type regression model, which is also shown in the figure. In the equation shown within the figure, (x) refers to the temperature in degrees Celsius, T(°C), while (y) refers to the membrane length in meters, L(cm). Therefore,

$$\boldsymbol{L(\mathrm{cm}) = 3.0364 \times 10^{6}\, T(^{\circ}\mathrm{C})^{-1.5676}} \qquad (12)$$

Thus, the temperature is an instrumental variable in limiting the membrane length (for a given target hydrogen recovery) to less than 25% of its base value. Thus, it is equally instrumental to increase the hydrogen recovery for a given geometric length.

Preprints.org (www.preprints.org) | NOT PEER-REVIEWED | Posted: 26 March 2025 doi:10.20944/preprints202503.1980.v1

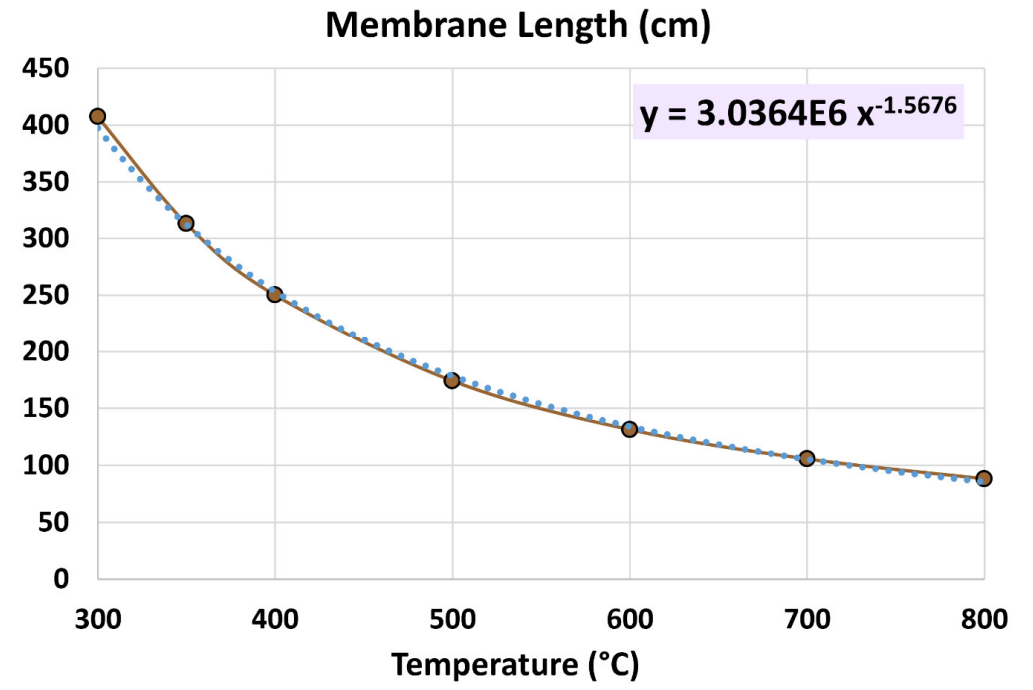

Figure 7. Membrane length as a function of the temperature in the membrane reactor.

Figure 8 shows the influence of the temperature on the second hydrogen permeation metric, which is the average hydrogen permeation mass flux. There is an almost linear increase with temperature, which can be described by the following linear regression model:

$$\bar{M}_{H2}(\mathbf{kg/m^2.hr}) = -\mathbf{1.4491} + \mathbf{0.0084087}\,\boldsymbol{T}(\mathbf{°C}) \qquad (13)$$

with an (R^2) value of 0.9990. This value that accompanies the linear regression equation is called the coefficient of determination. It helps in evaluating the goodness of the regression fit, with a perfect fit having a value of 1.0 [156,157]. Therefore, the provided regression model is almost perfect within the examined range of temperatures.

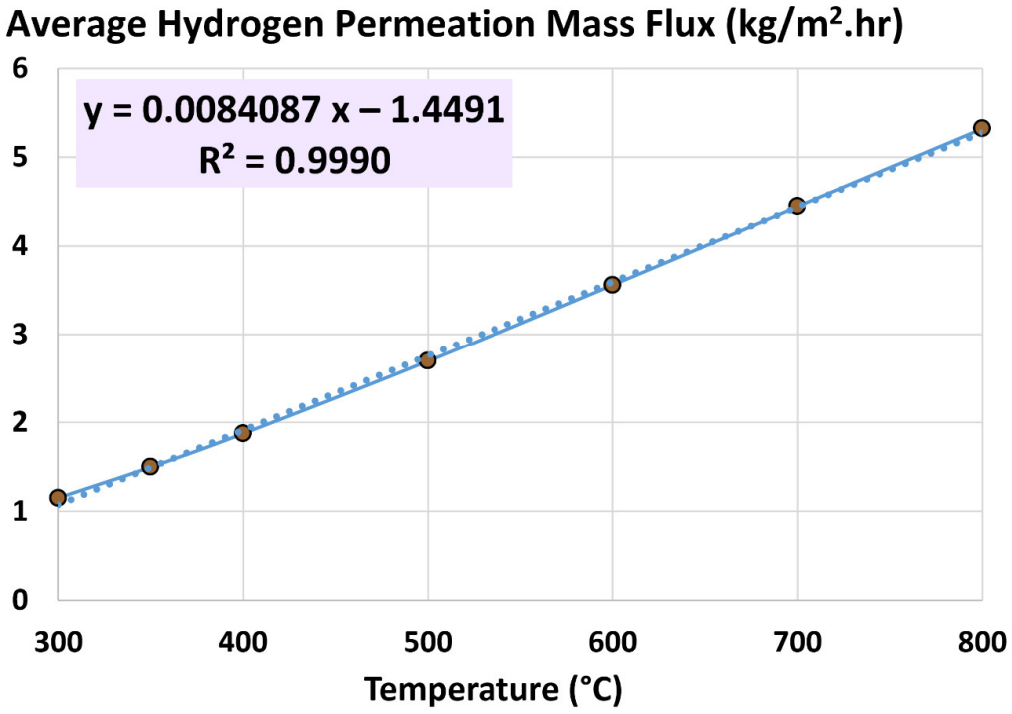

 doi:10.20944/preprints202503.1980.v1

Figure 8. Average hydrogen permeation mass flux as a function of the temperature in the membrane reactor.

Thus, the temperature is an instrumental variable to improve the permeation flux. This is justified by the increase in the actual local permeance when the temperature increases, following an Arrhenius-type dependence; which actually appears in different fields other than the current application of hydrogen permeation (such as chemical reaction rates [158]).

The third hydrogen permeation metric, which is the logarithmic mean pressure-square-root difference (LMPD) maintains its base values due to fixed inlet and outlet pressures. Therefore, its implicit dependence on the temperature is not manifested. Similarly, the left-end pressure-square-root difference, $(\Delta P_{H2}^{0.5})_{LHS,1}$, and the right-end pressure-square-root difference, $(\Delta P_{H2}^{0.5})_{RHS,n}$ remain the same when the temperature of the membrane reactor is varied while fixing the inlet and outlet pressures. Thus, they maintain their base values. Therefore, there is no need to visualize these three variables in a dedicated figure with the temperature being the independent variable (because they would simply appear as three straight horizontal lines in such a figure).

The lack of influence of temperature on this permeation metric is valid, due to fixing the pressures in all the cases while changing only the temperatures.

Figure 9 shows how the fourth and fifth hydrogen permeation metrics change as the temperature increases. These metrics are the global apparent permeance and the efficiency factor, respectively. In addition, the figure also includes the actual local permeance. While both the actual (local) permeance and the global apparent permeance increase nonlinearly with the temperature, their ratio remains constant at the base value of 67.09%. Because their ratio is, by definition, the efficiency factor; the efficiency factor remains constant at its base value when the operational temperature of the palladium membrane reactor module increases. The increase of the permeance values follows exactly an exponential function of the form

$$k' \text{ or } k'_{app}\left(\text{mol/m}^2\text{.s.Pa}^{0.5}\right) \propto e^{-\mu/(T(°C)+273.15)} \qquad (14)$$

where (μ) is a constant, being the activation energy divided by the universal gas constant (E/R̄).

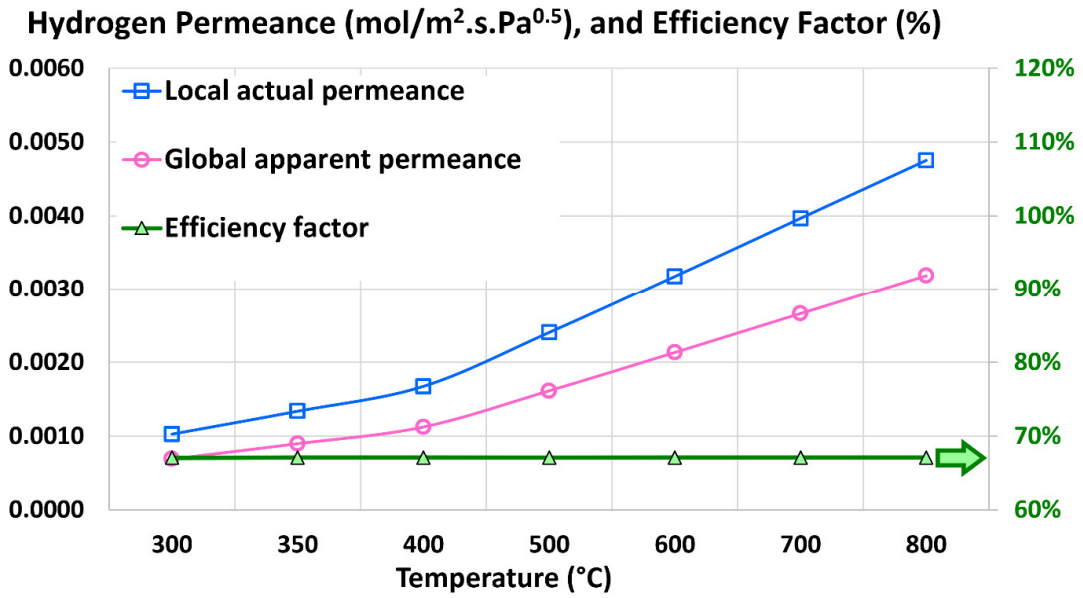

Figure 9. Local actual permeance, global apparent permeance, and efficiency factor as functions of the temperature in the membrane reactor.

Therefore, while increasing the temperature leads to better permeance, it is useless for improving the efficiency factor.

5.3. Influence of Retentate Pressure

Preprints.org (www.preprints.org) | NOT PEER-REVIEWED | Posted: 26 March 2025 doi:10.20944/preprints202503.1980.v1

After exploring the role of the temperature as a design variable to improve permeation in a membrane reactor, this subsection explores the similar role of the retentate pressure. The retentate pressure is varied in a discrete manner, leading to a number of pressures higher than the base value of 40 atm (absolute). The base value and seven additional absolute retentate pressures are:

1. 40 atm (base)
2. 45 atm
3. 50 atm
4. 60 atm
5. 70 atm
6. 80 atm
7. 100 atm
8. 120 atm

The goal here is to investigate the relation between this retentate pressure and the five performance metrics. The other two design variables (temperature and permeate pressure) are kept at their base values (300 °C and 20 atm absolute, respectively).

Figure 10 shows the influence of the retentate pressure on the first hydrogen permeation metric, which is the membrane length. Similar to the observed relation with the temperature, there is a favorable nonlinear decline in the membrane length as the retentate pressure increases. This relation can be described by the following fifth-order polynomial:

$$(\mathbf{cm}) = \mathbf{4.43331 \times 10^{-5}}\, r^4 - \mathbf{0.015423}\, r^3 + \mathbf{2.0356}\, r^2 - \mathbf{119.74}\, r + \mathbf{2812.2} \quad (15)$$

where (r) refers to the retentate absolute pressure, expressed in atm, P_{Ret}(atm, absolute). The retentate pressure was found to be an instrumental variable in limiting the membrane length (for a given target hydrogen recovery) to less than 25% of its base value at about 110 atm(absolute). In other words, it can be utilized to increase the hydrogen recovery for a given geometric length.

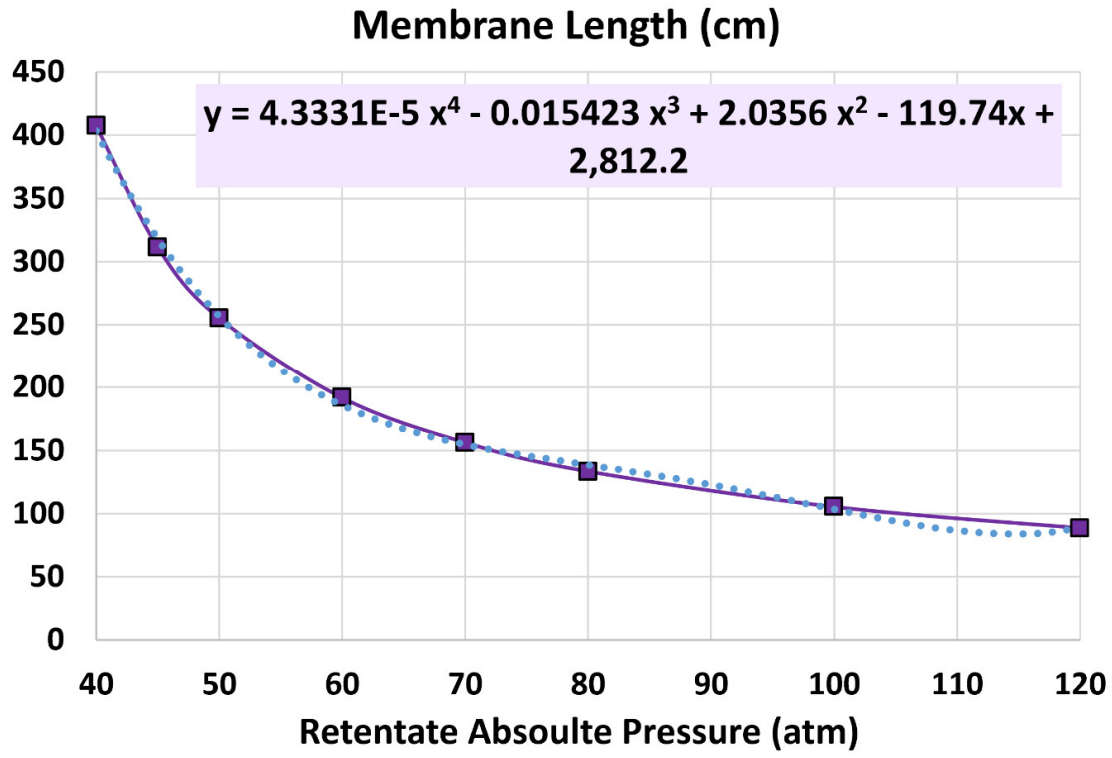

Figure 10. Membrane length as a function of the retentate pressure in the membrane reactor.

Figure 11 shows the influence of the retentate pressure on the second hydrogen permeation metric, which is the average hydrogen permeation mass flux. There is an approximate linear increase with pressure, which can be described by the following linear regression model:

 doi:10.20944/preprints202503.1980.v1

$$\bar{M}_{H2}(\mathbf{kg/m^2.hr}) = -0.75288 + 0.051720\, P_{Ret}(\mathbf{atm, absolute}) \quad (16)$$

with an (R^2) value of 0.9931, which is close to the perfect value of 1.0. Thus, the retentate pressure is useful for improving the permeation flux. This is justified by the increase in the driving force for permeation when the retentate pressure increases, due to the resulting proportional increase in the hydrogen partial pressure in the retentate stream.

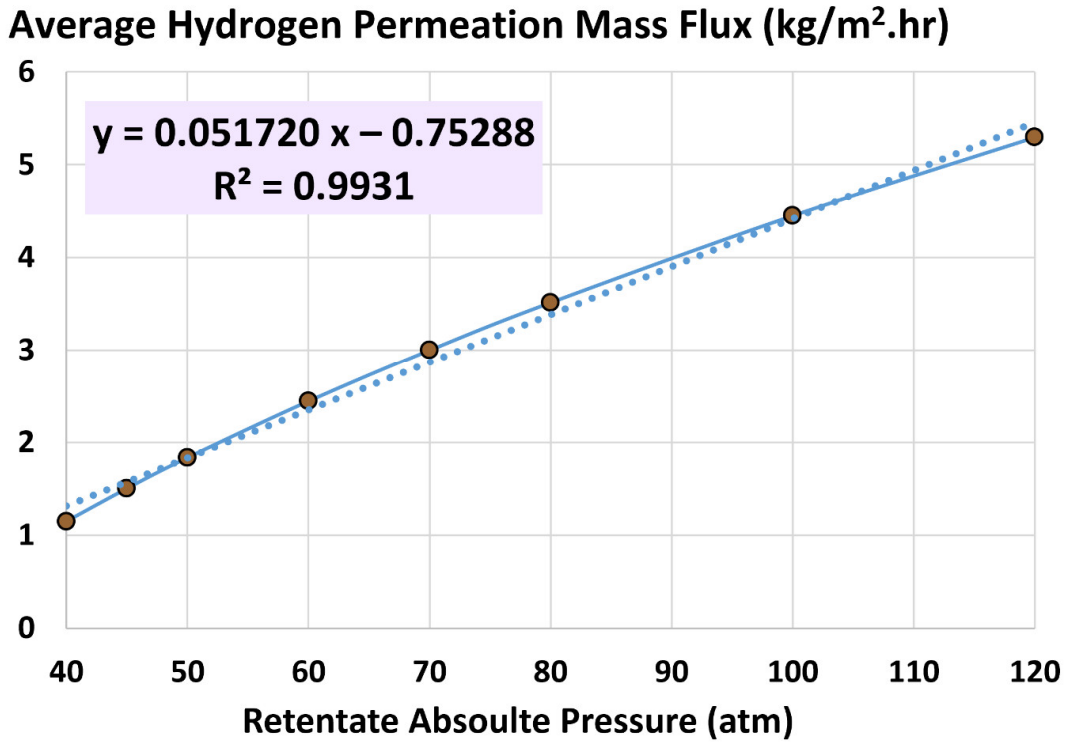

Figure 11. Average hydrogen permeation mass flux as a function of the retentate pressure in the membrane reactor.

Figure 12 shows that the third hydrogen permeation metric (log mean pressure-square-root difference - LMPD) increases logarithmically with the retentate pressure. The relation between the log mean pressure-square-root difference and the absolute pressure of the retentate stream over the range of considered pressures can be approximated as the following logarithmic function:

$$\mathbf{LMPD}\left(\mathbf{Pa^{0.5}}\right) = 442.40 \ln(P_{Ret}(\mathbf{atm, absolute})) - 1,412.6 \quad (17)$$

At an absolute retentate pressure of about 47 atm, the left-end pressure-square-root difference and the right-end pressure-square-root difference are equal, and become matching with the log mean pressure-square-root difference. The gap between the left-end and right-end pressure-square-root difference becomes larger as the retentate pressure increases.

 doi:10.20944/preprints202503.1980.v1

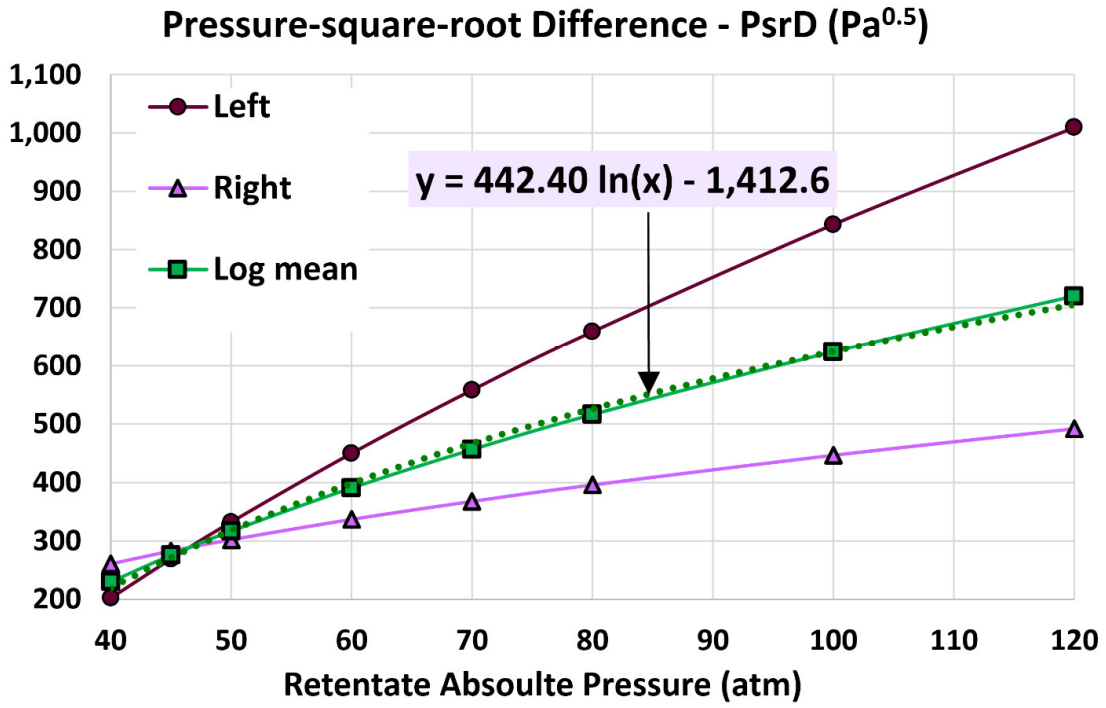

Figure 12. Pressure-square-root difference at the left end of the membrane reactor (x = 0), pressure-square-root difference at the right end of the membrane reactor (x = L), and log mean pressure-square-root difference (LMPD) as functions of the retentate pressure in the membrane reactor.

Figure 13 shows how the global apparent permeance and the efficiency factor change as the retentate pressure increases. The actual local permeance is fixed at its base value of 10.263×10^{-4} mol/m^2.s.Pa$^{0.5}$, but the apparent global permeance increases slightly as the retentate pressure increases, and it approaches the actual local permeance at high retentate pressure. The efficiency factor increases from its base value of 67.09% at 40 atm(absolute) to 98.71% at 120 atm(absolute).

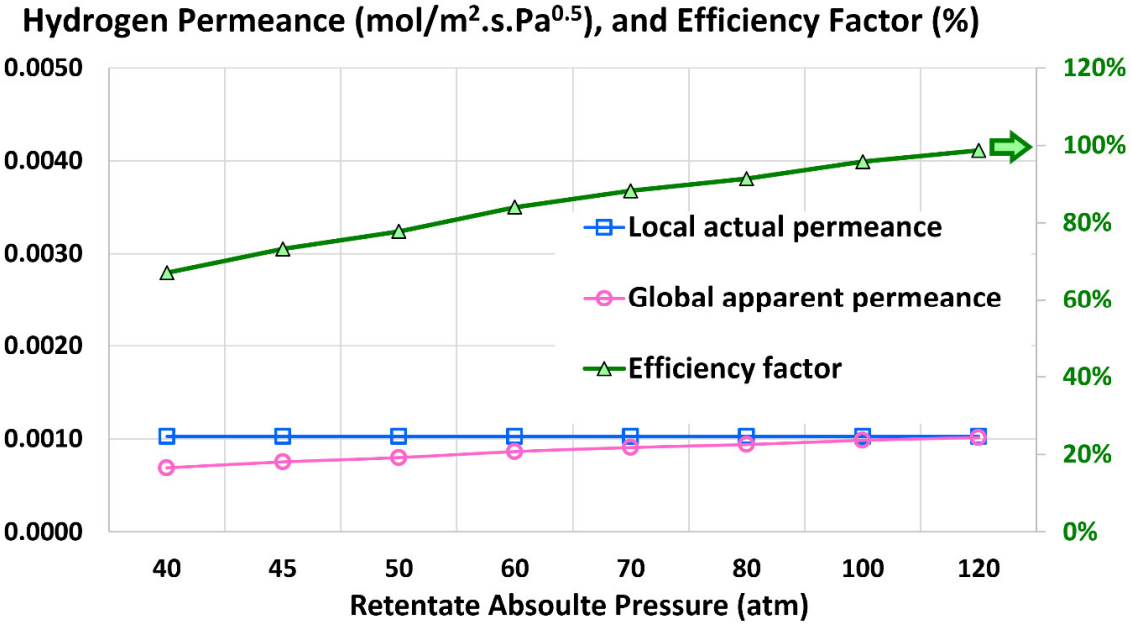

Figure 13. Local actual permeance, global apparent permeance, and efficiency factor as functions of the retentate pressure in the membrane reactor.

5.4. Influence of Permeate Pressure

 doi:10.20944/preprints202503.1980.v1

In this subsection, the impact of the permeate pressure (the last design variable considered in this study) on the permeation metrics is discussed. Seven additional simulations with different values of the absolute permeate pressure were conducted with the aim of capturing the trend of the permeation performance when the permeate pressure decreases from the base value of 20 atm (absolute) to a small value near the absolute vacuum (0 atm absolute) [159,160]. The base value and seven additional absolute permeate pressures are:

1. 20 atm (base)
2. 17.5 atm
3. 15 atm
4. 10 atm
5. 5 atm
6. 1 atm
7. 0.5 atm
8. 0.2 atm

The other two design variables (temperature and retentate pressure) are kept at their base values (300 °C and 40 atm absolute, respectively). Unlike the temperature and the retentate pressure, where larger values than the base values were investigated, smaller values of permeate pressures are investigated here for seeking better permeation, since this permeation pressure has a resistive effect for permeation (not a supportive effect as the temperature and the retentate pressure).

Figure 14 shows the influence of the permeate pressure on the first hydrogen permeation metric, which is the membrane length. There is a nonlinear (nearly exponential) increase in the membrane length as the retentate pressure increases. This relation can be described by the following regression model:

$$\boldsymbol{L(\mathrm{cm}) = 93.105\, e^{0.07192\, P_{Per}(\mathrm{atm,absolute})}} \quad (18)$$

Although manipulating the permeate pressure can reduce the membrane length (for a given target hydrogen recovery) to less than 25% of its base value (which was also achievable by manipulating the temperature or the retentate pressure), a partial vacuum is needed to achieve this, with pressures below the normal atmospheric pressure of 1 atm. This imposes complications and expense, and may not be acceptable. However, the reduction in the permeate pressure within more realistic values (like 10 atm, absolute) has still a favorable effect, and the membrane length can decrease to less than half of its base value by halving the absolute permeate pressure.

 doi:10.20944/preprints202503.1980.v1

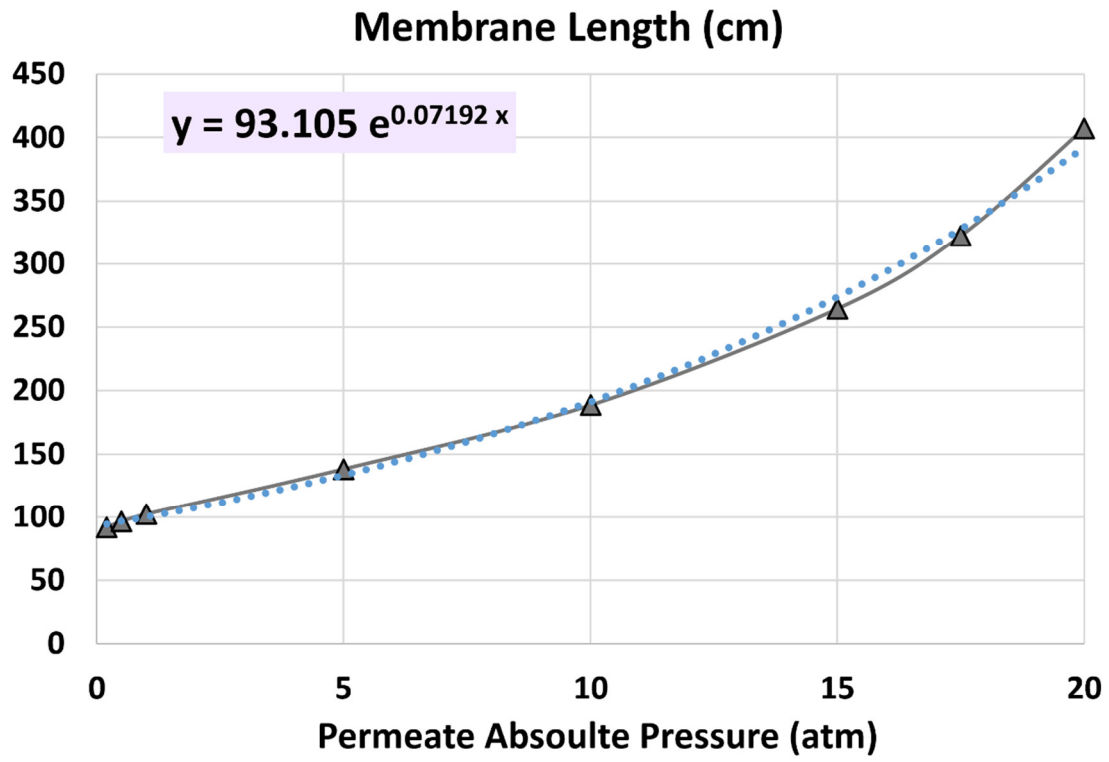

Figure 14. Membrane length as a function of the permeate pressure in the membrane reactor.

Figure 15 shows the influence of the permeate pressure on the second hydrogen permeation metric, which is the average hydrogen permeation mass flux. There is approximately an exponential decline in the average hydrogen permeation mass flux as the permeate pressure increases. This can be described by the following nonlinear regression model:

$$\bar{M}_{H2}(\mathbf{kg/m^2.hr}) = \mathbf{5.0339}\, e^{-0.07192\, P_{Per}(\mathrm{atm,absolute})} \quad (19)$$

If the absolute permeate pressure can be reduced to half of its base value, the average hydrogen permeation mass flux can be intensified to more than twice its base value. At the base case (with the base absolute permeate pressure of 20 bar), the average hydrogen permeation mass flux is 1.15054 kg/m².hr. This increases to 2.48568 kg/m².hr at an absolute permeate pressure of 10 bar (which is an increase by a multiplicative factor of 2.160 compared to the base case), and increases further to 5.10756 kg/m².hr at an absolute permeate pressure of 0.2 bar (which is an increase by a multiplicative factor of 4.439 compared to the base case).

 doi:10.20944/preprints202503.1980.v1

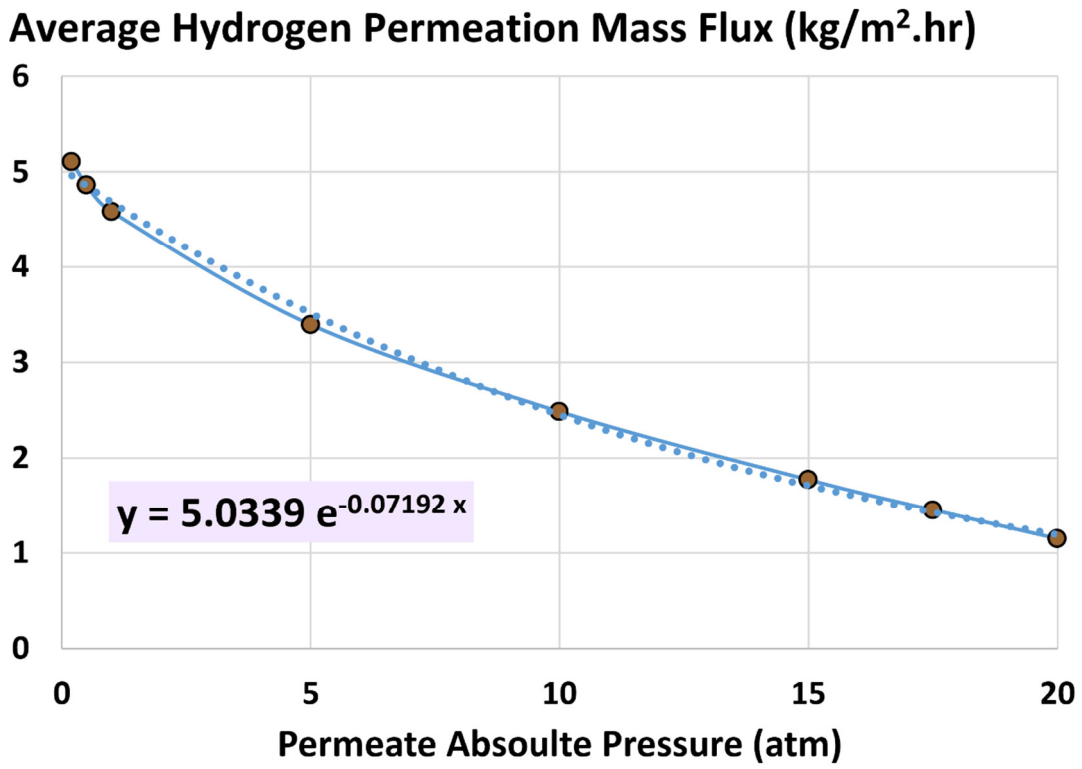

Figure 15. Average hydrogen permeation mass flux as a function of the permeate pressure in the membrane reactor.

Figure 16 shows that the third hydrogen permeation metric (log mean pressure-square-root difference) increases logarithmically with retentate pressure. The relation between the pressure-square-root (LMPD) and the absolute pressure of the permeate stream over the range of considered pressures can be approximated as an exponential function as

$$\mathbf{LMPD}\left(\mathbf{Pa}^{0.5}\right) = \mathbf{571.05}\, e^{-0.04471\, P_{Per}(\mathrm{atm,absolute})} \quad (20)$$

Below the absolute permeate pressure of about 17.5 atm, the left-end pressure-square-root difference is larger than the right-end pressure-square-root difference, which is reversed at higher permeate pressures.

 doi:10.20944/preprints202503.1980.v1

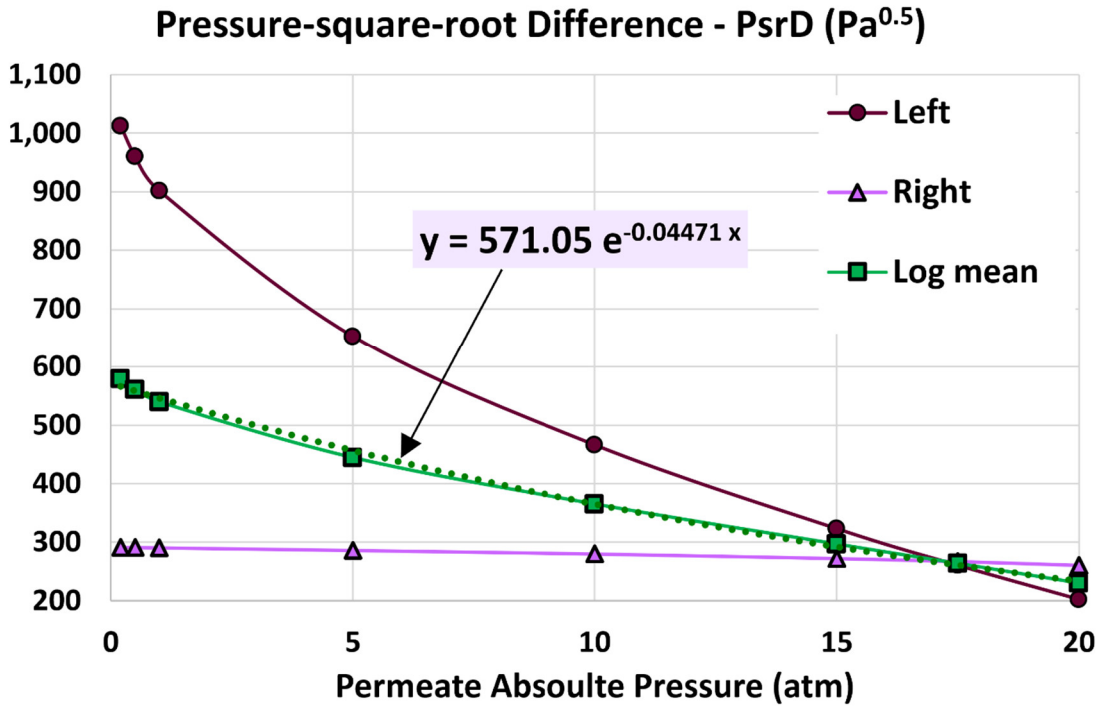

Figure 16. Pressure-square-root difference at the left end of the membrane reactor (x = 0), pressure-square-root difference at the right end of the membrane reactor (x = L), and log mean pressure-square-root difference (LMPD) as functions of the permeate pressure in the membrane reactor.

Figure 17 shows how the global apparent permeance and the efficiency factor decrease as the permeate pressure increases. The actual local permeance is fixed at its base value of 10.263×10^{-4} mol/m^2.s.Pa$^{0.5}$, but the apparent global permeance decreases from a value higher than the actual local permeance (thus, an efficiency factor above 100%) at very low permeate pressures to a value smaller than the actual local permeance as the permeate pressure increases (thus, an efficiency factor below 100%) as the absolute permeate pressure is increases beyond about 5 atm. Specifically, the efficiency factor reaches 102.53% and 118.43% at absolute permeate pressures of 5 atm and 0.2 atm, respectively (compared to the base value of 67.09% at 20 atm, absolute).

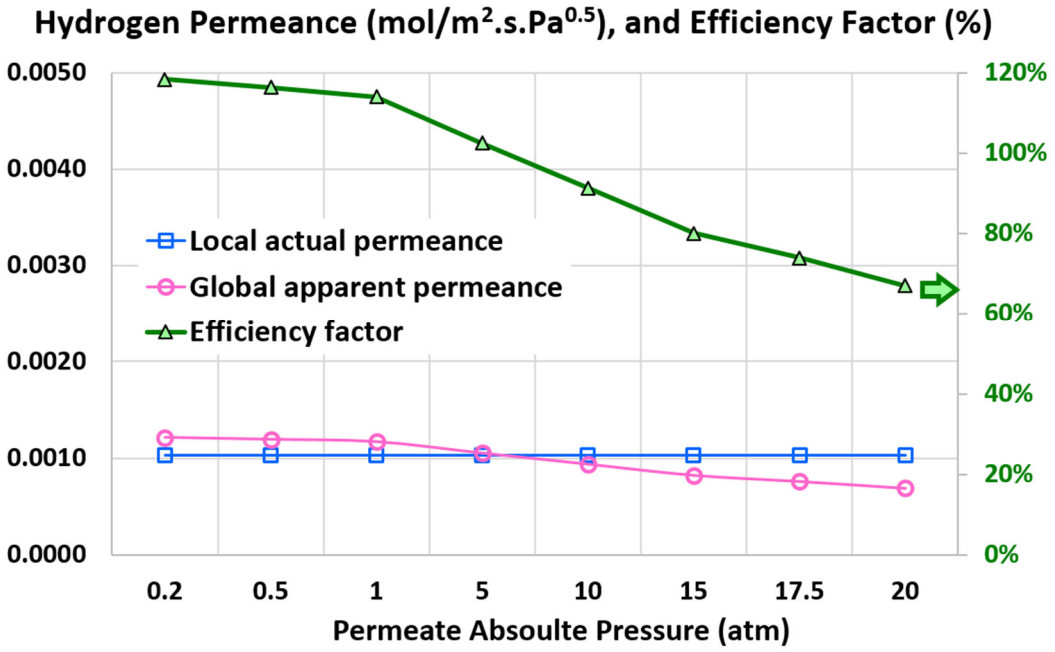

 doi:10.20944/preprints202503.1980.v1

Figure 17. Local actual permeance, global apparent permeance, and efficiency factor as functions of the permeate pressure in the membrane reactor.

5.5. Profiles with Extreme Design Variables

The final method to highlight the general impacts of the three design variables (temperature, retentate pressure, and permeate pressure) on the hydrogen permeation within a generic palladium membrane reactor is by contrasting some longitudinal profiles when the membrane reactor operates at the extreme values assigned to each design variable while keeping the other two design variables at their base values.

This means contrasting results from three different simulations with the following conditions in Table 6:

Table 6. Some details about the base case (reference simulation).

Extreme case number	Temperature	Absolute retentate pressure	Absolute permeate pressure
1	800 °C (1,472.00 °F)	40.0 atm (587.84 psia)	20.0 atm (293.92 psia)
2	300 °C (572.00 °F)	120.0 atm (1,763.5 psia)	20.0 atm (293.92 psia)
3	300 °C (572.00 °F)	40.0 atm (587.84 psia)	0.20 atm (2.9392 psia)

The cumulative hydrogen recovery profiles for the three extreme cases are contrasted in Figure 18. The left-end value (0%) and the right-end value (95%) are implicitly imposed by the enforced inlet or outlet conditions. Thus, all profiles should coincide at both the left and right edges of the membrane reactor, but they can deviate in the intermediate zone. The cumulative hydrogen recovery for the extreme temperature shows more linearity than the other two profiles, with the extreme permeate pressure corresponding to a curved profile, resembling a second-order function of the normalized membrane coordinate (x/L), with a gradually declining slope as x/L increases. The extreme retentate pressure simulation shows an intermediate behavior between the other two extreme cases, in terms of the cumulative hydrogen recovery profiles.

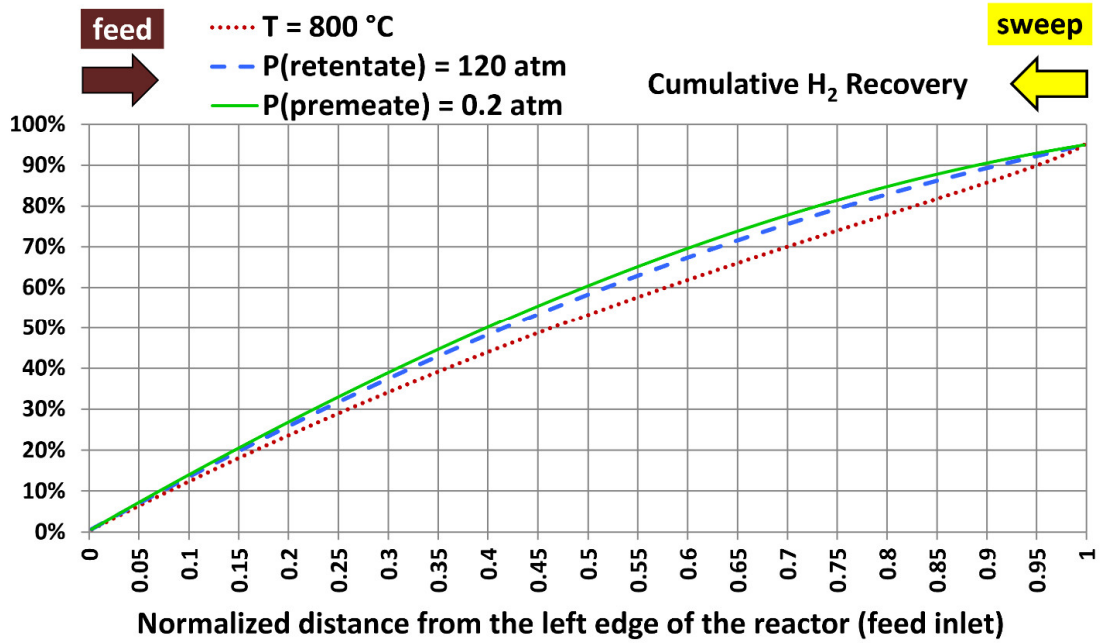

Figure 18. Commutative hydrogen recovery with the extreme values considered for the temperature, absolute retentate pressure, and absolute permeate pressure.

 doi:10.20944/preprints202503.1980.v1

This behavior is better explained by visualizing the segmental contribution to the total hydrogen recovery for these three extreme cases in Figure 19. While the profile for the extreme temperature is not horizontal, it first decreases and then increases, making it behave as if changing around a uniform mean value. Thus, the cumulative value (integration of the profile) should be close to a straight upward line as shown earlier. On the other hand, the extreme permeate pressure causes a nearly linear declining profile for the segmental hydrogen recovery, which when integrated, gives a nearly quadratic profile as shown before. The extreme retentate pressure simulation shows an intermediate behavior between the other two extreme cases, as noted earlier.

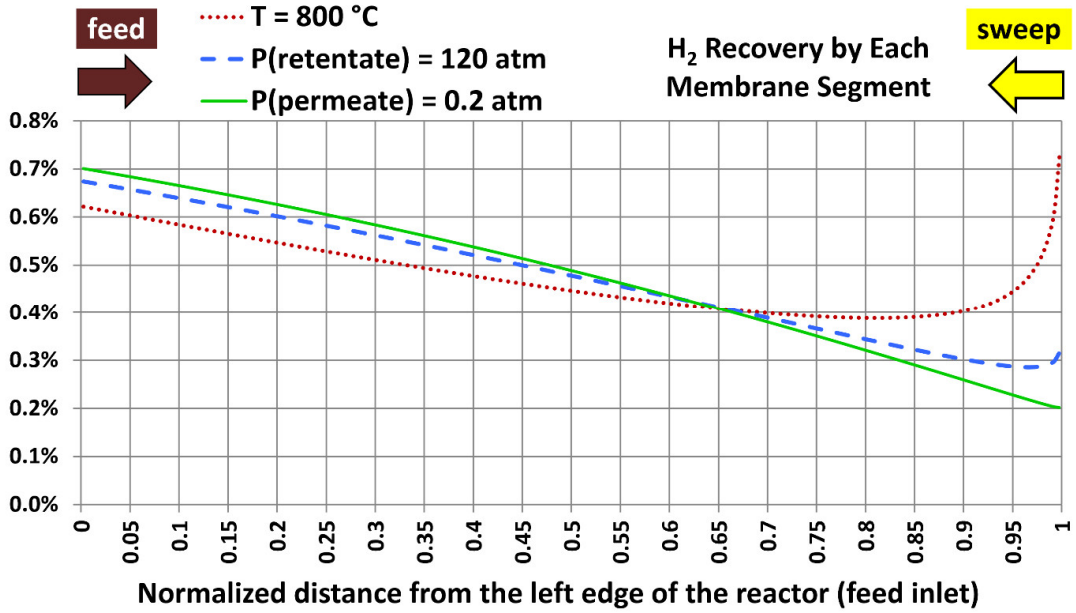

Figure 19. Segmental hydrogen recovery with the extreme values considered for the temperature, absolute retentate pressure, and absolute permeate pressure.

The hydrogen mole fractions in the retentate stream and in the permeate stream for the three extreme cases are contrasted in Figures 20 and 21, respectively. The simulation with the extreme permeate pressure shows a regular variation for both streams. The simulation with the extreme temperature shows an accelerated decline in the hydrogen mole fractions in both streams as the coordinate x approaches the right end (permeate inlet, retentate exit). This can be attributed to the rapidly elevated segmental hydrogen recovery in this region, after steadily declining in the left part of the membrane reactor. Again, the extreme retentate pressure simulation shows an intermediate behavior between the other two extreme cases.

 doi:10.20944/preprints202503.1980.v1

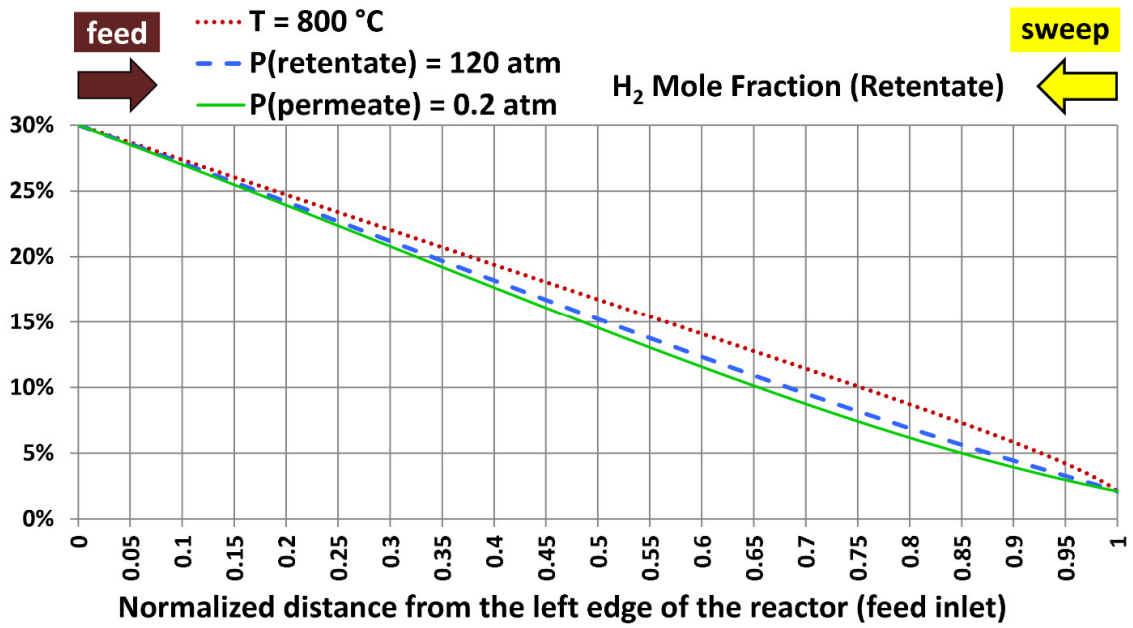

Figure 20. Hydrogen mole fraction in the retentate stream with the extreme values considered for the temperature, absolute retentate pressure, and absolute permeate pressure.

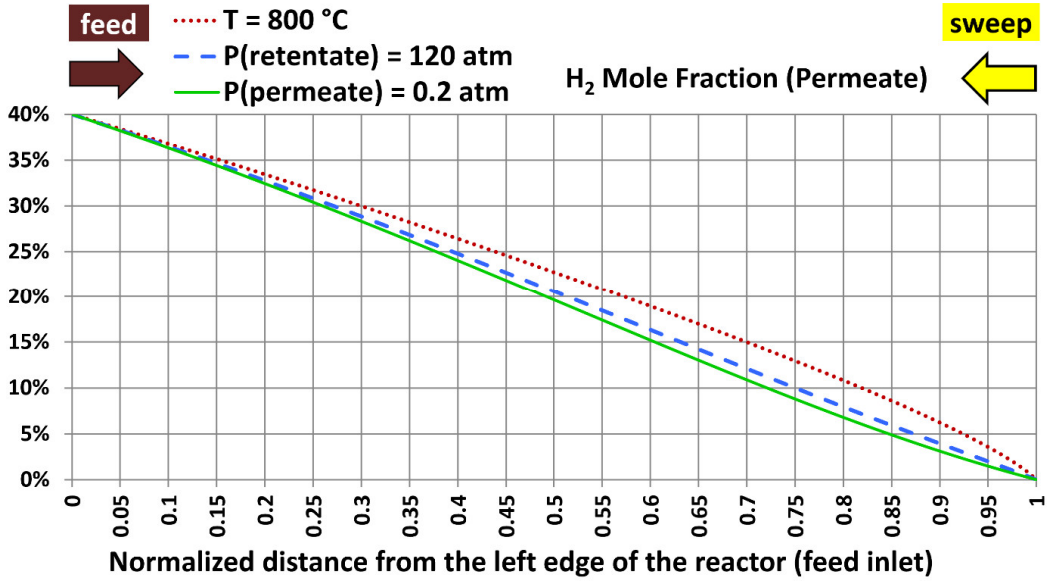

Figure 21. Hydrogen mole fraction in the permeate stream with the extreme values considered for the temperature, absolute retentate pressure, and absolute permeate pressure.

6. Discussion

This section addresses two topics. First, it briefly discusses how some of the presented components in this study can add new insight to the literature and fill a potential gap in it. Second, it addresses the question of whether or not the results are limited to ideal gases.

The contribution of this work to the fields of energy systems, computational modeling, hydrogen production, and carbon capture includes presenting a simple plug-flow reactor computational model for the membrane-based hydrogen separation, which takes a short time to give rough predictions as a precursor of time-consuming three-dimensional computational fluid dynamics (CFD) models. The simple plug-flow reactor model developed here can be automated using spreadsheet software without resorting to complicated computer programming or expensive simulation packages. The

 doi:10.20944/preprints202503.1980.v1

model was checked by comparing cases with different spatial resolutions. The model uses a predictor-corrector approach in the computation, where an initial value (in a predictor step) is refined (in a corrector step) to yield the final value at each segment of the segmented reactor. An apparent lack of such a model in the literature is one of the motivations for disseminating this study. The present study also demonstrates examples of consolidated metrics for comparing and judging the permeation performance of hydrogen. This can guide researchers when analyzing or interpreting similar problems. In addition, the study describes the impact of three different design variables on the hydrogen permeation performance, accompanied by good-fit regression models. This step helps in having a broad estimation of the advantage of manipulating each of these variables, which can be weighed against the expenses or practical difficulty in a realistic setting, thus helping in selecting optimum operational conditions.

While inspecting the steps of the proposed numerical membrane-based permeation model for hydrogen, confusion may arise regarding any restriction of applicability to gases that obey the ideal-gas law (ideal-gas equation of state). This can be caused because the proposed model has steps (steps e and j) where the molar flux of permeating hydrogen through the palladium membrane (with the unit: mol/m^2.s, which is moles per square meter per second) was expressed as a standard-temperature-pressure volume flow rate (with the unit: scc/min or sccm, which is standard cubic centimeters per minute). In particular, in step e, the conversion constant (22,711 scc/mol) was explicitly utilized, and it was derived earlier in Equation (6) using the ideal-gas equation of state. However, such restriction does not exist. The standard cubic centimeter (scc) for a gas is simply another unit of the amount of substance, like the mole (mol) unit and the kilomole (kmol) unit. All the numerical values used to derive the conversion constant (22,711 scc/mol) represent universal constants themselves. These values are: the universal gas constant ($\bar{R}$ = 8.3145 J/mol.K), the units multiplier (10^6 cm^3/m^3), the standard absolute temperature (273.15 K), and the standard pressure (10^5 Pa). Therefore, the unit (scc) is always linearly related to the unit (mol) through a fixed multiplication factor, that is independent of the type of gas, the operating temperature, and the operating pressure. The use of scc in the model (rather than mol for example) can be viewed as an arbitrary choice for compliance with others who use this unit for gaseous flow rates in academic, commercial, or governmental sectors [161–164], and for convenience due to dealing with larger numbers having many significant digits before the decimal point.

Some studies may adopt slightly different values for the standard temperature and standard pressure than those adopted here. For example, the pressure value of 1 atm (101,325 Pa) may be considered the standard pressure instead of 10^5 Pa [165–169]. In such a case, the conversion constant (22,711 scc/mol) derived here consequently should change slightly to 22,414 scc/mol (after multiplying 22,711 by 10^5 and dividing it by 101,325), but this does not invalidate the fact that the scc and the mol are two related units.

In relation to the aforementioned remark, Table 2 in the present study provides the inlet standard volume flow rate (in sccm) for the retentate stream. This value is what is needed as a boundary condition to start using the proposed numerical hydrogen permeation model. The same table provides also the equivalent mass flow rate (in kg/hr and lbm/hr). This mass flow rate is auxiliary information. It is not directly utilized in the proposed permeation model.

The deviation from the ideal gas condition (which is utilized in the current study) is expressed in terms of a non-dimensional number called compressibility factor or deviation factor, Z [170–176], defined as

$$\boldsymbol{Z = \frac{P}{\rho R T} = \frac{P v}{R T}} \qquad (21)$$

where (P) is the absolute pressure, (ϱ) is the density, (R) is the specific gas constant, (T) is the absolute temperature, and (v) is the specific volume (the reciprocal of the density).

For ideal gases, the compressibility factor is exactly 1 [177,178]. The more the deviation from the unity compressibility factor, the more the error resulting from using the ideal-gas law. The compressibility factor depends on the type of the gas, its temperature, and its pressure. Each gas has

 doi:10.20944/preprints202503.1980.v1

a characteristic temperature called the critical temperature or T_c [179–184], above which a vapor-liquid phase change becomes no longer observable. When the temperature of the gas is well above its critical point, this gas generally does not deviate significantly from being ideal, over a wide range of pressure [185,186]. All the simulations presented in the current study are at relatively high temperatures (from 300 °C to 800 °C, or 573.15 K to 1,073.15 K), which are much more than the critical temperature of all the four gases (H_2, CO, CO_2, N_2) included in all the simulations in the current study. The critical temperature of these gases ranges from 33.2 K for H_2 to 304.2 K for CO_2 [187–191]. Therefore, these gases are not expected to deviate largely from the ideal gas behavior in the performed simulations. For example, experiments showed that the compressibility factor for hydrogen at 75 °C (348.15 K) varies from 1.0024 at an absolute pressure of 4.5400 atm to 1.0455 at an absolute pressure of 85.269 atm [192]. As another example to support the ideal-gas assumption adopted in the current study, reported calculations based on the Reference Fluid Thermodynamic and Transport Properties Database (REFPROP) [60] of the United States National Institute of Standards and Technology (NIST) [193] showed that the compressibility factor for hydrogen at 125 °C (398.15 K) varies from 1.0005 at an absolute pressure of 0.9869 atm to 1.0481 at an absolute pressure of 98.69 atm [194].

7. Conclusions

A discrete plug-flow reactor model was established for simulating the one-dimensional isothermal permeation of hydrogen through palladium membranes, and was applied for separating hydrogen from a pressurized hot syngas stream. The model assumed a shell-and-tube cross-section for estimating the exact membranes area. A set of inlet conditions for the feed syngas and an inlet sweep nitrogen were established. Also, a target hydrogen recovery of 95% and a target hydrogen mole fraction of 40% at the permeate exit were enforced. The required membrane length was computed to achieve these targets. The model consisted of 200 segments, with each segment having a length of about 2 cm. After a validity test, it was found that this spatial segmentation is adequate.

Then, the impact of three operational variables was investigated, when varied individually starting from the reference values such that better hydrogen permeation can be obtained. These design variables are the temperature, retentate-side pressure, and permeate-side pressure. For quantitative evaluation of the hydrogen permeation improvement, five assessment metrics were discussed, including the apparent global permeance and the efficiency factor. Linear or nonlinear regression models were provided for the membrane length, the average permeation mass flux, and the log mean pressure-square-root difference. In addition, the one-dimensional profiles of some permeation-related quantities (such as the segmental hydrogen recovery) at the extreme value of each design variable were contrasted. The present study can serve as a rough guide for palladium-based hydrogen separation, showing designers some potential gains in hydrogen permeation by manipulating some operational conditions. The designers may then seek an optimum compromise between the expected gain and the incurred complications or implementation costs.

Considering the relative changes in the three investigated design variables and the dependent hydrogen permeation metrics in 21 simulations (one reference simulation and 20 additional ones), temperature is the most effective variable for improving the permeation performance. The retentate pressure comes in the second place. The permeate pressure is the least powerful way to improve hydrogen permeation.

Funding: This research received no funding.

Data Availability Statement: Data elements and parameters used in this study are described and contained within the manuscript itself.

Conflicts of Interest: The author declares that they have no known competing financial interests or personal relationships that could have appeared to influence the work reported in this paper.

 doi:10.20944/preprints202503.1980.v1

Appendix A. Continuous Plug-Flow Reactor Modeling

This appendix gives a brief description of modelling a continuous plug-flow reactor (PFR).

The Center for Chemical Process Safety (CCPS) within the American Institute of Chemical Engineers (AIChE) defines a plug-flow reactor (PFR) as "A tubular reactor where the feed is continuously introduced at one end and the products continuously removed from the other end. The concentration / temperature in the reactor is not uniform" [195]. This definition is commended for being generic enough to cover different varieties of the PFR model, based on specific sets of assumptions implied. It can be added that in a plug-flow reactor, the plug-like flow of substance does not have any mixing along the axial direction (no axial mixing between different 'plugs' of material) [196].

If the axial (longitudinal) axis is denoted by (x), the concentration of the ith species is denoted by (C_i), the volumetric reaction rate is denoted by (r), the linear velocity is denoted by (u), and the stoichiometric coefficient of the ith species is denoted by (ν_i), then the following partial differential equation governs the temporal and spatial evolution of the concentration along the PFR [197]:

$$\frac{\partial C_i}{\partial t} + \frac{\partial C_i}{\partial x} = \frac{1}{u}\,\nu_i\, r \qquad \text{(A.1)}$$

If the flow is assumed to be steady, the above partial differential equation (PDE) is reduced to an ordinary differential equation (ODE) as:

$$\frac{dC_i}{dx} = \frac{1}{u}\,\nu_i\, r \qquad \text{(A.2)}$$

Furthermore, if the reaction is first order, which means that the reaction rate depends linearly on the concentration of only one reactant [198], then the axial gradient of the concentration (C) of that reacting species in the PFR becomes

$$\frac{dC}{dx} = -\frac{1}{u}\,k\,C \qquad \text{(A.3)}$$

where (k) is the rate coefficient of the reaction, which can depend on the absolute temperature (T) following an exponential profile [199], such that

$$k = k_0\, e^{-\varepsilon T} \qquad \text{(A.4)}$$

where (k_0) and (ε) are constants.

Appendix B. Modelling Hydrogen Permeation

Appendix B.1. Segmental Plug-Flow Reactor

Hydrogen permeation through a palladium membrane is a nonlinear phenomenon [200], which can be understood and investigated through numerical simulations rather than simple symbolic expressions [201]. For simulating the hydrogen permeation in the simplified hydrogen membrane reactor (HMR), piece-wise constant profiles are utilized to replace the continuous distributions along the membrane reactor; and no partial differential equations or sources of unsteadiness are involved. The membrane reactor is divided into (n) segments, having a small thickness and a constant cross-section. Each segment is assumed to have a uniform gas composition in either the permeate stream or in the retentate stream, and a uniform permeation flux. The flow is steady (time-independent), with a feed syngas entering the reactor from the left end (and leaving the reactor from the right end after losing 95% of its hydrogen moles), and a sweep gas entering the reactor from the right end (and leaving the reactor from the left end after gaining the same amount of hydrogen lost from the syngas, reaching a composition of 40% hydrogen and 60% nitrogen, by mole or volume). Such a segmental approach for handling the one-dimensional evolution of the permeation process along the membrane reactor resembles a discretized version of a plug-flow reactor, PFR [202]. Instead of having infinitely small segments (or plugs) in a true PFR, these segments here are finite. Also, instead of solving ordinary differential equations to find the composition distribution as a function of the longitudinal coordinate as in true PFR problems [203], a numerical approach based on a nonlinear mathematical framework involving scalar algebraic equations only, without a need to solve vector equations or to process matrices [204] is used to describe that composition in adjacent segments, by ensuring

 doi:10.20944/preprints202503.1980.v1

continuity of the permeate flow and the retentate flow at the interfaces of each pair of adjacent segments. The hydrogen permeation occurs through the palladium membranes from the retentate to the permeate, with the permeation rate approximated as being uniform (having the same value) within each segment, but it can change from one segment to another. In other words, the smoothly changing permeation rate is discretized and approximated as a piecewise-constant function. Similarly, the driving force for hydrogen permeation (which stems from the partial pressures of hydrogen in the retentate and the permeate sides) is also approximated as a piecewise-constant function.

Appendix B.2. Modeling Algorithm

Figure A1 explains the segmentation of the hypothetical hydrogen membrane reactor (HMR). It shows a portion of its left end, with the two most-left segments. The left end of the membrane reactor is where the coordinate (x) is assigned the value zero. Because the segmental plug-flow reactor (PFR) model is aimed to capture the hydrogen permeation with no consideration of the flow pattern, only the membrane surface is of concern here, because it is where permeation occurs. No gradients are allowed in the direction perpendicular to the longitudinal axis (thus, no gradients perpendicular to the membrane surface). The membrane is simplified in the figure as a cylindrical surface, separating the permeate stream (inside) from the retentate stream (outside).

The left-hand side (LHS) of the first segment is the left end of the entire membrane (where x = 0).

The LHS of other segments (all segments except the first one) is the right-hand side (RHS) of the previous segment located to its left.

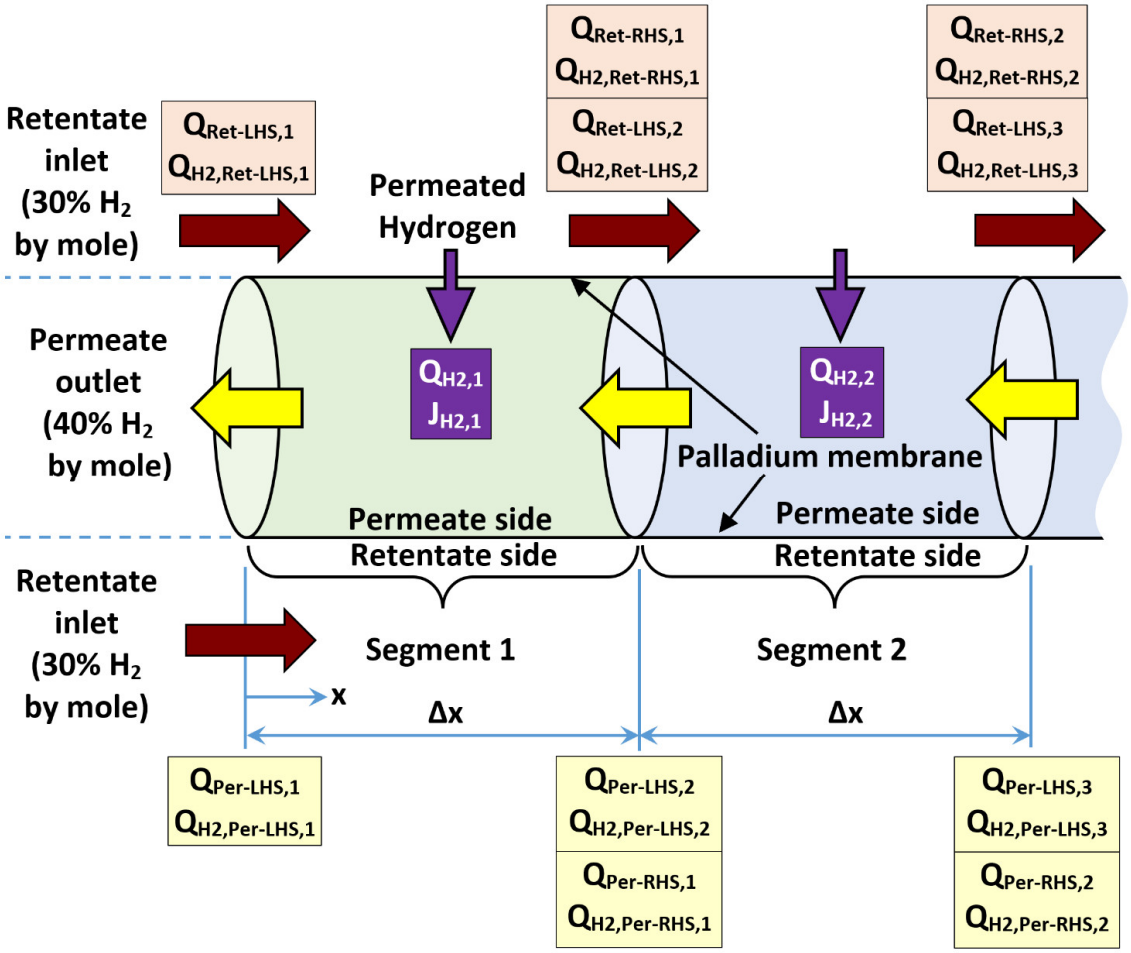

Figure A1. Illustration of the segments of the membrane reactor near its left end.

 doi:10.20944/preprints202503.1980.v1

The index number (i) for a segment can take the value from (1) for the first segment at the left edge of the membrane reactor to (n) for the last segment at the right edge of the membrane reactor. The algorithm for calculating the segment-wise composition in the permeate and the retentate streams for a generic segment is provided below.

a) Start with a known hydrogen mole fraction in the retentate at the LHS ($X_{H2,Ret-LHS,i}$), standard volume flow rate of retentate at the LHS ($Q_{Ret-LHS,i}$), hydrogen mole fraction of permeate at the LHS ($X_{H2,Per-LHS,i}$), and standard volume flow rate of permeate at the LHS ($Q_{Per-LHS,i}$) of the segment (say segment number i).

For this step, there are two routes of calculations

For the first segment (i = 1), implement the inlet conditions and the target mole fraction as follows:

$$\boldsymbol{X_{H2,Ret-LHS,1} = 30\%\ (\text{specified inlet condition})} \quad \text{(B.1)}$$

$$\boldsymbol{Q_{Ret-LHS,1} = 970,068\ \text{sccm}\ (\text{specified inlet condition})} \quad \text{(B.2)}$$

$$\boldsymbol{Q_{H2,Ret-LHS,1} = X_{H2,Ret-LHS,1}\, Q_{Ret-LHS,1}} \quad \text{(B.3)}$$

In the last equation, the product ($X_{H2,Ret-LHS,1}$ $Q_{Ret-LHS,1}$) gives the standard volume flow rate of the hydrogen content in the feed syngas.

$$\boldsymbol{X_{H2,Per-LHS,1} = 40\%\ (\text{specified target})} \quad \text{(B.4)}$$

$$\boldsymbol{Q_{Per-LHS,1} = \frac{\beta\, Q_{H2,Ret-LHS,1}}{X_{H2,Per-LHS,1}}} \quad \text{(B.5)}$$

In the last equation, multiplying the standard volume flow rate of the hydrogen content in the feed syngas ($Q_{H2,Ret-LHS,1}$) by the target hydrogen recovery (β) gives the target standard volume flow rate of the hydrogen content in the permeate stream as it exits the membrane reactor from its left end. Dividing this value further by the target mole fraction of the exiting permeate stream ($X_{H2,Per-LHS,1}$) gives the target standard volume flow of the exiting permeate stream ($Q_{Per-LHS,1}$), which is composed of molecular hydrogen and molecular nitrogen. Performing these calculations gives $Q_{Per-LHS,1}$ = 691,173 sccm.

For other segments except the first one (i = 2, 3, … n), the connectivity condition of the segments (interfacing condition) can be used as follows:

$$\boldsymbol{X_{H2,Ret-LHS,i} = X_{H2,Ret-RHS,i-1}} \quad \text{(B.6)}$$

$$\boldsymbol{Q_{Ret-LHS,i} = Q_{Ret-RHS,i-1}} \quad \text{(B.7)}$$

$$\boldsymbol{Q_{H2,Ret-LHS,i} = Q_{H2,Ret-RHS,i-1}} \quad \text{(B.8)}$$

$$\boldsymbol{X_{H2,Per-LHS,i} = X_{H2,Per-RHS,i-1}} \quad \text{(B.9)}$$

$$\boldsymbol{Q_{Per-LHS,i} = Q_{Per-RHS,i-1}} \quad \text{(B.10)}$$

where the values of ($X_{H2,Ret-RHS,i-1}$), ($Q_{Ret-RHS,i-1}$), ($Q_{H2,Ret-RHS,i-1}$), ($X_{H2,Per-RHS,i-1}$), and ($Q_{Ret-RHS,i-1}$) should be available from the analysis of the previous segment (numbered i–1).

b) Compute ($Q_{H2,Per-LHS,i}$), which is the standard volume flow rate of the hydrogen content in the permeate stream at the LHS of the current segment being analyzed (say segment i), as follows:

$$\boldsymbol{Q_{H2,Per-LHS,i} = X_{H2,Per-LHS,i}\, Q_{Per-LHS,i}} \quad \text{(B.11)}$$

c) Compute $(\Delta P_{H2}^{0.5})_{LHS,i}$, which is the difference in the partial pressures of hydrogen raised to the power of 0.5 (this difference is the driving force for hydrogen permeation through the palladium membrane) at the LHS of the current segment being analyzed (say segment i), as follows:

$$\boldsymbol{\left(\Delta P_{H2}^{0.5}\right)_{LHS,i} = \left(X_{H2,Ret-LHS,i}\, P_{Ret}\right)^{0.5} - \left(X_{H2,Per-LHS,i}\, P_{Per}\right)^{0.5}} \quad \text{(B.12)}$$

where (P_{Ret}) is the absolute pressure of the retentate stream, and (P_{Per}) is the absolute pressure of the permeate stream. Since the retentate stream is assumed to have a constant pressure, there is no need to add details (a subscript index) about the location for its value to be used in the above equation. The same reason justifies not specifying a particular location for the permeate pressure.

 doi:10.20944/preprints202503.1980.v1

d) Compute ($\not{J}_{H2,i}$), which is a predicted (first-iteration) segment-level molar flux of permeating hydrogen through the palladium membrane based on the conditions at LHS of the current segment being analyzed (say segment i), as follows:

$$\not{J}_{H2,i} = k' \left(\Delta P_{H2}^{0.5} \right)_{LHS,i} \qquad \text{(B.13)}$$

This predicted flux value is an initial estimation, based on LHS conditions only. In a subsequent step of the present algorithm, it is refined by including the effects of RHS conditions of the segment.

The above equation is referred to as the Richardson equation [205,206]. It is based on applying both Fick's law for diffusion of hydrogen atoms across the metal membrane, and Sieverts' law relating the concentration of the hydrogen atoms in the metal membrane (equilibrium between gaseous hydrogen molecules next to the metal membrane and dissociated hydrogen atoms in the metal membrane) to the square root of the partial pressure of the adjacent molecular hydrogen gas [207–209]. The factor (k') is an ideal (or local, or actual) permeance for hydrogen permeation. It is the product of the Fick's diffusion coefficient (for the hydrogen atoms' diffusion across the metal membrane) and the Sieverts' solubility constant (the Sieverts' law constant for the dissociation of an H_2 molecule into two H atoms), and divided by the thickness of the metal membrane. In the current model, the factor (k') is calculated as

$$k' = \frac{A}{\delta} e^{-E/(\bar{R}T)} \qquad \text{(B.14)}$$

where (A) is a pre-exponential factor for hydrogen permeation, (δ) is the thickness of the palladium membrane, (E) is an activation energy for hydrogen permeation, and (T) is the absolute temperature (in kelvins). The values of (A) and (E) used here are [210,211]

$$A = 2.2 \times 10^{-7} \text{ mol/m/s/Pa}^{0.5}$$

$$E = 15{,}670 \text{ J/mol}$$

with $\bar{R}$ = 8.3145 J/mol.K, the value of ($E/\bar{R}$) in the above equation becomes 1,884.7 K.

The thickness of the palladium membrane is set to 80 μm, which is considered a reasonable value [212,213].

e) Convert the LHS-based first-iteration molar flux ($\not{J}_{H2,i}$) to a predicted (first-iteration) segment-level standard volume flow rate of permeating hydrogen ($\not{Q}_{H2,i}$) for the current segment being analyzed (say segment i).

This temporary standard volume flow rate value is an initial estimation, based on LHS conditions only. In a subsequent step of the present algorithm, it is refined by including effects of RHS conditions. It is computed as follows:

$$\not{Q}_{H2,i} = \lambda \not{J}_{H2,i} A_{seg} \qquad \text{(B.15)}$$

where (A_{seg}) is the membrane surface area in one segment, and (λ) is a constant that arises from a necessary unit conversion, as follows:

$$\lambda = 22{,}711 \frac{\text{scc}}{\text{mol}} \, 60 \frac{\text{s}}{\text{min}} \qquad \text{(B.16)}$$

where (scc) stands for (standard cubic centimeters). This gives $\lambda = 1.36266 \times 10^6$ scc.s/mol.min.

When computing the segmental membrane area, the envisioned tubes layout in the shell-and-tube design and its specified dimensions become necessary.

If the tube diameter is designated by the symbol (d), and the length of the entire membrane reactor is designated by the symbol (L), then for eight tubes and (n) segments, the length of a single segment is

$$\Delta x = \frac{L}{n} \qquad \text{(B.17)}$$

and the membrane area within a single segment is

$$A_{seg} = 8 \, \Delta x \, \pi \, d \qquad \text{(B.18)}$$

where (π = 3.14159) is the traditional mathematical constant.

f) Compute ($\not{X}_{H2,Ret\text{-}RHS,i}$) and ($\not{X}_{H2,Per\text{-}RHS,i}$), which are predicted (first-iteration) mole fractions of hydrogen in the retentate stream and the permeate stream, respectively at the RHS of the current segment being analyzed (say segment i), as follows:

 doi:10.20944/preprints202503.1980.v1

$$\boldsymbol{X_{H2,Ret-RHS,i}} = \frac{\boldsymbol{Q_{H2,Ret-LHS,i} - Q_{H2,i}}}{\boldsymbol{Q_{Ret-LHS,i} - Q_{H2,i}}} \quad \text{(B.19)}$$

$$\boldsymbol{X_{H2,Per-RHS,i}} = \frac{\boldsymbol{Q_{H2,Per-LHS,i} - Q_{H2,i}}}{\boldsymbol{Q_{Per-LHS,i} - Q_{H2,i}}} \quad \text{(B.20)}$$

g) Compute $(\Delta P_{H2}^{0.5})_{RHS,I}$, which is the difference in the partial pressures of hydrogen raised to the power of 0.5 (as the driving force for hydrogen permeation) at the RHS of the current segment being analyzed (say segment i), as follows:

$$\left(\boldsymbol{\Delta P_{H2}^{0.5}}\right)_{\boldsymbol{RHS,i}} = \left(\boldsymbol{X_{H2,Ret-RHS,i}\, P_{Ret}}\right)^{\boldsymbol{0.5}} - \left(\boldsymbol{X_{H2,Per-RHS,i}\, P_{Per}}\right)^{\boldsymbol{0.5}} \quad \text{(B.21)}$$

h) Compute $(\Delta P_{H2}^{0.5})_i$, which is the difference in the partial pressures of hydrogen raised to the power of 0.5 assigned to the current segment being analyzed (say segment i). It is taken as the arithmetic average of the LHS value and the RHS value, as follows:

$$\left(\boldsymbol{\Delta P_{H2}^{0.5}}\right)_{\boldsymbol{i}} = \boldsymbol{0.5}\left(\left(\boldsymbol{\Delta P_{H2}^{0.5}}\right)_{\boldsymbol{LHS,i}} + \left(\boldsymbol{\Delta P_{H2}^{0.5}}\right)_{\boldsymbol{RHS,i}}\right) \quad \text{(B.22)}$$

i) Compute $(J_{H2,i})$, which is a corrected (second-iteration) segment-level molar flux of permeating hydrogen through the palladium membrane, which includes driving forces for permeation at both sides of the current segment being analyzed (say segment i), as follows:

$$\boldsymbol{J_{H2,i}} = \boldsymbol{k'}\left(\boldsymbol{\Delta P_{H2}^{0.5}}\right)_{\boldsymbol{i}} \quad \text{(B.23)}$$

j) Convert the corrected, segment-level molar flux $(J_{H2,i})$ to a corresponding updated (refined) segment-level standard volume flow rate of permeating hydrogen $(Q_{H2,i})$ for the current segment being analyzed (say segment i), as follows:

$$\boldsymbol{Q_{H2,i}} = \boldsymbol{\lambda\, J_{H2,i}\, A_{seg}} \quad \text{(B.24)}$$

This is considered the final representation of the segment-level permeation of hydrogen.

k) Compute $(R_{H2,i})$, which is the hydrogen recovery due to the current segment being analyzed (say segment i), as follows:

$$\boldsymbol{R_{H2,i}} = \boldsymbol{Q_{H2,i}/Q_{H2,Ret-LHS,1}} \quad \text{(B.25)}$$

The denominator $(Q_{H2,Ret-LHS,1})$ in the previous equation is basically the standard volume flow rate of hydrogen in the inlet feed syngas. Thus, it is the standard volume flow of hydrogen available for permeation.

The segmental contribution to the overall recovery $(R_{H2,i})$ can help in studying the distribution of the permeation, and thus identifying portions of the membrane reactor that are more effective than others.

l) Optional: Compute $(\widehat{R}_{H2,i})$, which is the cumulative hydrogen recovery, due to all previous segments of the membrane reactor in addition to the current segment being analyzed (say segment i), as follows:

$$\boldsymbol{\widehat{R}_{H2,i}} = \boldsymbol{\sum_{m=1}^{i} R_{H2,i}} \quad \text{(B.26)}$$

While this value is not necessary for continuing the calculation process, it is part of the data visualization of results here. It is thus beneficial to explain how it is obtained.

m) Compute $(Q_{Ret-RHS,i})$ and $(Q_{H2,Ret-RHS,i})$, which are the standard volume flow rate of the retentate stream and the hydrogen content in that retentate stream, respectively at the RHS of the current segment being analyzed (say segment i), as follows:

$$\boldsymbol{Q_{Ret-RHS,i}} = \boldsymbol{Q_{Ret-LHS,i} - Q_{H2,i}} \quad \text{(B.27)}$$

$$\boldsymbol{Q_{H2,Ret-RHS,i}} = \boldsymbol{Q_{H2,Ret-LHS,i} - Q_{H2,i}} \quad \text{(B.28)}$$

n) Compute $(X_{H2,Ret-RHS,i})$, which is the corrected (second-iteration) mole fraction of hydrogen in the retentate stream at the RHS of the current segment being analyzed (say segment i), as follows:

$$\boldsymbol{X_{H2,Ret-RHS,i}} = \boldsymbol{Q_{H2,Ret-RHS,i}/Q_{Ret-RHS,i}} \quad \text{(B.29)}$$

 doi:10.20944/preprints202503.1980.v1

o) Compute ($Q_{Per-RHS,i}$) and ($Q_{H2,Per-RHS,i}$), which are the standard volume flow rate of the permeate stream and the hydrogen content in that permeate stream, respectively at the RHS of the current segment being analyzed (say segment i), as follows:

$$\boldsymbol{Q_{Per-RHS,i} = Q_{Per-LHS,i} - Q_{H2,i}} \quad \text{(B.30)}$$

$$\boldsymbol{Q_{H2,Per-RHS,i} = Q_{H2,Per-LHS,i} - Q_{H2,i}} \quad \text{(B.31)}$$

p) Compute ($X_{H2,Per-RHS,i}$), which is the corrected (second-iteration) mole fraction of hydrogen in the permeate stream at the RHS of the current segment being analyzed (say segment i), as follows:

$$\boldsymbol{X_{H2,Per-RHS,i} = Q_{H2,Per-RHS,i}/Q_{Per-RHS,i}} \quad \text{(B.32)}$$

q) Set the obtained RHS conditions of the current segment being analyzed (say segment i) as LHS conditions at the next adjacent segment to be analyzed (segment i+1), and repeat the computation procedure sequentially for all remaining segments until the last membrane segment (segment n).

The following values should be obtained for each segment:

- $(\Delta P_{H2}^{0.5})_{LHS,i}$
- ~~J~~$_{H2,i}$
- ~~Q~~$_{H2,i}$
- ~~X~~$_{H2,Ret-RHS,i}$ and ~~X~~$_{H2,Per-RHS,i}$
- $(\Delta P_{H2}^{0.5})_{RHS,i}$
- $(\Delta P_{H2}^{0.5})_{i}$
- $J_{H2,i}$
- $Q_{H2,i}$
- $R_{H2,i}$
- Optional: $\hat{R}_{H2,i}$
- $Q_{Ret-RHS,i}$ and $Q_{H2,Ret-RHS,i}$
- $X_{H2,Ret-RHS,i}$
- $Q_{Per-RHS,i}$ and $Q_{H2,Per-RHS,i}$
- $X_{H2,Per-RHS,i}$

r) Compute ($\hat{R}_{H2,n}$), which is the cumulative hydrogen recovery at the last segment. It is the overall hydrogen recovery by the entire membrane reactor, and it is obtained by simply adding the segment-level hydrogen recovery ($R_{H2,i}$) for all the (n) segments of the membrane reactor. The total cumulative value is itself the target hydrogen recovery (β). Therefore

$$\boldsymbol{\beta \text{ or } \hat{R}_{H2,n} = \sum_{m=1}^{n} R_{H2,i}} \quad \text{(B.33)}$$

The hydrogen recovery is an important success criterion not only from the chemical perspective, but also from an economic perspective. A higher hydrogen recovery leads to a lower cost per unit mass of hydrogen produced [214,215].

In the presented algorithm, the length of the entire membrane (L) is a nonlinear function of the overall hydrogen recovery (β). Since (β) is fixed at a desired value of 95% (in all the simulation cases of this study), a matching membrane length (L) should be obtained. Solving such a non-linear system of equations is achieved here using the (Goal Seek) tool in the Microsoft Excel software program. This tool is useful only when the equation or system of equations relates a single independent variable to a single dependent variable [216]. This condition is satisfied in the segmented plug-flow reactor problems here, with the independent variable being the membrane length, and the dependent variable being the hydrogen recovery.

References

1. D.A. Bell, B.F. Towler, M. Fan, Coal gasification and its applications, William Andrew/Elsevier, Oxford, U.K., 2011.

 doi:10.20944/preprints202503.1980.v1

2. O.A. Marzouk, E.D. Huckaby, Assessment of syngas kinetic models for the prediction of a turbulent nonpremixed flame, in: Fall Meet. East. States Sect. Combust. Inst. 2009, College Park, Maryland, USA, 2009: pp. 726–751. https://doi.org/10.31219/osf.io/87n2x.
3. N. Couto, A. Rouboa, V. Silva, E. Monteiro, K. Bouziane, Influence of the Biomass Gasification Processes on the Final Composition of Syngas, Energy Procedia 36 (2013) 596–606. https://doi.org/10.1016/j.egypro.2013.07.068.
4. A. Jayanarasimhan, R.M. Pathak, A.M. Shivapuji, L. Rao, Tar Formation in Gasification Systems: A Holistic Review of Remediation Approaches and Removal Methods, ACS Omega 9 (2024) 2060–2079. https://doi.org/10.1021/acsomega.3c04425.
5. [National Energy Technology Laboratory of the United States Department of Energy] NETL, Reactions & Transformations, (2022). https://netl.doe.gov/research/coal/energy-systems/gasification/gasifipedia/reaction-transformations (accessed May 5, 2022).
6. S.M. Frolov, K.S. Panin, V.A. Smetanyuk, Gasification of Liquid Hydrocarbon Waste by the Ultra-Superheated Mixture of Steam and Carbon Dioxide: A Thermodynamic Study, Energies 17 (2024) 2126. https://doi.org/10.3390/en17092126.
7. M. Talmadge, M. Biddy, A. Dutta, S. Jones, A. Meyer, Syngas Upgrading to Hydrocarbon Fuels Technology Pathway, National Renewable Energy Laboratory (NREL), and Pacific Northwest National Laboratory (PNNL) of the United States Department of Energy (DoE)., 2013. https://www.nrel.gov/docs/fy13osti/58052.pdf (accessed May 31, 2024).
8. S. Lin, M. Harada, Y. Suzuki, H. Hatano, Hydrogen production from coal by separating carbon dioxide during gasification, Fuel 81 (2002) 2079–2085. https://doi.org/10.1016/S0016-2361(02)00187-4.
9. Stork, Syngas Fired Steam Boiler, (2022). https://www.stork.com/en/client-cases/syngas-fired-steam-boiler (accessed May 6, 2022).
10. S. Suxing, X. Yu, J. Li, X. Liu, L. Sui, J. Zhang, Z. Fu, Y. Shao, Effects of Hydrogen Addition on the Thermal Performance and Emissions of Biomass Syngas Combustion in a Horizontal Boiler, Energies 17 (2024) 2632. https://doi.org/10.3390/en17112632.
11. O.A. Marzouk, Portrait of the Decarbonization and Renewables Penetration in Oman's Energy Mix, Motivated by Oman's National Green Hydrogen Plan, Energies 17 (2024) 4769. https://doi.org/10.3390/en17194769.
12. M.S. Timilsina, Y. Chaudhary, A.K. Shah, S.P. Lohani, R. Bhandari, B. Uprety, Syngas composition analysis for waste to methanol production: Techno-economic assessment using machine learning and Aspen plus, Renew. Energy 228 (2024) 120574. https://doi.org/10.1016/j.renene.2024.120574.
13. M. Cavo, M. Rivarolo, L. Gini, L. Magistri, An advanced control method for fuel cells - Metal hydrides thermal management on the first Italian hydrogen propulsion ship, Int. J. Hydrog. Energy 48 (2023) 20923–20934. https://doi.org/10.1016/j.ijhydene.2022.07.223.
14. O.A. Marzouk, Expectations for the Role of Hydrogen and Its Derivatives in Different Sectors through Analysis of the Four Energy Scenarios: IEA-STEPS, IEA-NZE, IRENA-PES, and IRENA-1.5°C, Energies 17 (2024) 646. https://doi.org/10.3390/en17030646.
15. P. Halder, M. Babaie, F. Salek, N. Haque, R. Savage, S. Stevanovic, T.A. Bodisco, A. Zare, Advancements in hydrogen production, storage, distribution and refuelling for a sustainable transport sector: Hydrogen fuel cell vehicles, Int. J. Hydrog. Energy 52 (2024) 973–1004. https://doi.org/10.1016/j.ijhydene.2023.07.204.
16. O.A. Marzouk, Zero Carbon Ready Metrics for a Single-Family Home in the Sultanate of Oman Based on EDGE Certification System for Green Buildings, Sustainability 15 (2023) 13856. https://doi.org/10.3390/su151813856.
17. H. Liu, H. Lu, H. Hu, CO_2 capture and mineral storage: State of the art and future challenges, Renew. Sustain. Energy Rev. 189 (2024) 113908. https://doi.org/10.1016/j.rser.2023.113908.
18. M. Bakirci, Smart city air quality management through leveraging drones for precision monitoring, Sustain. Cities Soc. 106 (2024) 105390. https://doi.org/10.1016/j.scs.2024.105390.
19. O.A. Marzouk, Compilation of Smart Cities Attributes and Quantitative Identification of Mismatch in Rankings, J. Eng. 2022 (2022) 5981551. https://doi.org/10.1155/2022/5981551.

 doi:10.20944/preprints202503.1980.v1

20. O.A. Marzouk, Adiabatic Flame Temperatures for Oxy-Methane, Oxy-Hydrogen, Air-Methane, and Air-Hydrogen Stoichiometric Combustion using the NASA CEARUN Tool, GRI-Mech 3.0 Reaction Mechanism, and Cantera Python Package, Eng. Technol. Appl. Sci. Res. 13 (2023) 11437–11444. https://doi.org/10.48084/etasr.6132.
21. A. Jamrozik, K. Grab-Rogaliński, W. Tutak, Hydrogen effects on combustion stability, performance and emission of diesel engine, Int. J. Hydrog. Energy 45 (2020) 19936–19947. https://doi.org/10.1016/j.ijhydene.2020.05.049.
22. T. Xie, P. Wang, Analysis of NO formation in counter-flow premixed hydrogen-air flame, Trans. Can. Soc. Mech. Eng. 37 (2013) 851–859. https://doi.org/10.1139/tcsme-2013-0072.
23. O.A. Marzouk, Hydrogen Utilization as a Plasma Source for Magnetohydrodynamic Direct Power Extraction (MHD-DPE), IEEE Access 12 (2024) 167088–167107. https://doi.org/10.1109/ACCESS.2024.3496796.
24. J. Goldmeer, J. Catillaz, J. Donohue, Hydrogen as a fuel for gas turbines - A pathway to lower CO_2, General Electric (GE), 2022. https://www.ge.com/content/dam/gepower-new/global/en_US/downloads/gas-new-site/future-of-energy/hydrogen-fuel-for-gas-turbines-gea34979.pdf (accessed May 31, 2024).
25. S. Javoy, R. Mevel, C.E. Paillard, A study of N_2O decomposition rate constant at high temperature: Application to the reduction of nitrous oxide by hydrogen, Int. J. Chem. Kinet. 41 (2009) 357–375. https://doi.org/10.1002/kin.20401.
26. N.T. Weiland, P.A. Strakey, Global NOx Measurements in Turbulent Nitrogen-Diluted Hydrogen Jet Flames, in: San Diego, California, United States, 2007. https://www.osti.gov/biblio/913259 (accessed May 31, 2024).
27. O.A. Marzouk, Dataset of total emissivity for CO2, H2O, and H2O-CO2 mixtures; over a temperature range of 300-2900 K and a pressure-pathlength range of 0.01-50 atm.m, Data Brief (2025) 111428. https://doi.org/10.1016/j.dib.2025.111428.
28. I. Ghiat, T. Al-Ansari, A review of carbon capture and utilisation as a CO_2 abatement opportunity within the EWF nexus, J. CO2 Util. 45 (2021) 101432. https://doi.org/10.1016/j.jcou.2020.101432.
29. P. Madejski, K. Chmiel, N. Subramanian, T. Kuś, Methods and Techniques for CO_2 Capture: Review of Potential Solutions and Applications in Modern Energy Technologies, Energies 15 (2022) 887. https://doi.org/10.3390/en15030887.
30. R. Ruan, G. Wang, S. Li, M. Wang, H. Lin, H. Tan, X. Wang, F. Liu, The effect of alkali and alkaline earth metals (AAEMs) on combustion and PM formation during oxy-fuel combustion of coal rich in AAEMs, Energy 293 (2024) 130695. https://doi.org/10.1016/j.energy.2024.130695.
31. O.A. Marzouk, Radiant Heat Transfer in Nitrogen-Free Combustion Environments, Int. J. Nonlinear Sci. Numer. Simul. 19 (2018) 175–188. https://doi.org/10.1515/ijnsns-2017-0106.
32. T. Rajabloo, J. Valee, Y. Marenne, L. Coppens, W. De Ceuninck, Carbon capture and utilization for industrial applications, Energy Rep. 9 (2023) 111–116. https://doi.org/10.1016/j.egyr.2022.12.009.
33. O.A. Marzouk, Temperature-Dependent Functions of the Electron–Neutral Momentum Transfer Collision Cross Sections of Selected Combustion Plasma Species, Appl. Sci. 13 (2023) 11282. https://doi.org/10.3390/app132011282.
34. I. Donskoy, Techno-Economic Efficiency Estimation of Promising Integrated Oxyfuel Gasification Combined-Cycle Power Plants with Carbon Capture, Clean Technol. 5 (2023) 215–232. https://doi.org/10.3390/cleantechnol5010013.
35. O.A. Marzouk, Detailed and simplified plasma models in combined-cycle magnetohydrodynamic power systems, Int. J. Adv. Appl. Sci. 10 (2023) 96–108. https://doi.org/10.21833/ijaas.2023.11.013.
36. C. Dinca, N. Slavu, C.-C. Cormoş, A. Badea, CO_2 capture from syngas generated by a biomass gasification power plant with chemical absorption process, Energy 149 (2018) 925–936. https://doi.org/10.1016/j.energy.2018.02.109.
37. O.A. Marzouk, Technical review of radiative-property modeling approaches for gray and nongray radiation, and a recommended optimized WSGGM for CO2/H2O-enriched gases, Results Eng. 25 (2025) 103923. https://doi.org/10.1016/j.rineng.2025.103923.

38. A. Bhavsar, D. Hingar, S. Ostwal, I. Thakkar, S. Jadeja, M. Shah, The current scope and stand of carbon capture storage and utilization ~ A comprehensive review, Case Stud. Chem. Environ. Eng. 8 (2023) 100368. https://doi.org/10.1016/j.cscee.2023.100368.
39. B. Dziejarski, R. Krzyżyńska, K. Andersson, Current status of carbon capture, utilization, and storage technologies in the global economy: A survey of technical assessment, Fuel 342 (2023) 127776. https://doi.org/10.1016/j.fuel.2023.127776.
40. D.L. Tomasko, H. Li, D. Liu, X. Han, M.J. Wingert, L.J. Lee, K.W. Koelling, A Review of CO_2 Applications in the Processing of Polymers, Ind. Eng. Chem. Res. 42 (2003) 6431–6456. https://doi.org/10.1021/ie030199z.
41. A. Singh, V. Saini, S. Jain, A. Gour, Techno-Economic, Environmental, and Policy Perspectives of Carbon Capture to Fuel Technologies, Int. Res. J. Adv. Eng. Hub IRJAEH 2 (2024) 1387–1403. https://doi.org/10.47392/IRJAEH.2024.0192.
42. A.M. Bukar, M. Asif, Technology readiness level assessment of carbon capture and storage technologies, Renew. Sustain. Energy Rev. 200 (2024) 114578. https://doi.org/10.1016/j.rser.2024.114578.
43. H.J.K. Shabbani, M.R. Othman, S.K. Al- Janabi, A.R. Barron, Z. Helwani, H2 purification employing pressure swing adsorption process: Parametric and bibliometric review, Int. J. Hydrog. Energy 50 (2024) 674–699. https://doi.org/10.1016/j.ijhydene.2023.11.069.
44. A.P. Singh, S. Singh, S. Ganguly, A.V. Patwardhan, Steam reforming of methane and methanol in simulated macro & micro-scale membrane reactors: Selective separation of hydrogen for optimum conversion, J. Nat. Gas Sci. Eng. 18 (2014) 286–295. https://doi.org/10.1016/j.jngse.2014.03.008.
45. A.H. Kassi, T.A. Al-Hattab, A Review: Membrane Reactor for Hydrogen Production: Modeling and Simulation, Eng. Chem. 4 (2023) 17–31. https://doi.org/10.4028/p-XakNe1.
46. M. Omidifar, A. Akbar Babaluo, S. Jamshidi, H_2 permeance and surface characterization of a thin (2 μm) Pd-Ni composite membrane prepared by electroless plating, Chem. Eng. Sci. 283 (2024) 119370. https://doi.org/10.1016/j.ces.2023.119370.
47. P.F. Zito, A. Brunetti, G. Barbieri, Hydrogen concentration and purification by membrane process: A multistage analysis, Renew. Energy 218 (2023) 119243. https://doi.org/10.1016/j.renene.2023.119243.
48. V. Piemonte, L. Di Paola, M. De Falco, A. Iulianelli, A. Basile, Hydrogen production using inorganic membrane reactors, in: Adv. Hydrog. Prod. Storage Distrib., Elsevier, 2014: pp. 283–316. https://doi.org/10.1533/9780857097736.3.283.
49. O.A. Marzouk, 2030 Ambitions for Hydrogen, Clean Hydrogen, and Green Hydrogen, Eng. Proc. 56 (2023) 14. https://doi.org/10.3390/ASEC2023-15497.
50. T. Peters, A. Caravella, Pd-Based Membranes: Overview and Perspectives, Membranes 9 (2019) 25. https://doi.org/10.3390/membranes9020025.
51. V. Marcantonio, M. De Falco, M. Capocelli, E. Bocci, A. Colantoni, M. Villarini, Process analysis of hydrogen production from biomass gasification in fluidized bed reactor with different separation systems, Int. J. Hydrog. Energy 44 (2019) 10350–10360. https://doi.org/10.1016/j.ijhydene.2019.02.121.
52. W. Liemberger, M. Groß, M. Miltner, M. Harasek, Experimental analysis of membrane and pressure swing adsorption (PSA) for the hydrogen separation from natural gas, J. Clean. Prod. 167 (2017) 896–907. https://doi.org/10.1016/j.jclepro.2017.08.012.
53. L. Vermaak, H.W.J.P. Neomagus, D.G. Bessarabov, Hydrogen Separation and Purification from Various Gas Mixtures by Means of Electrochemical Membrane Technology in the Temperature Range 100–160 °C, Membranes 11 (2021) 282. https://doi.org/10.3390/membranes11040282.
54. K. Chang, Q. Li, Q. Li, Refrigeration cycle for cryogenic separation of hydrogen from coke oven gas, Front. Energy Power Eng. China 2 (2008) 484–488. https://doi.org/10.1007/s11708-008-0096-0.
55. T. Kangwanpongpan, D. Makarov, D. Cirrone, V. Molkov, LES model of flash-boiling and pressure recovery phenomena during release from large-scale pressurised liquid hydrogen storage tank, Int. J. Hydrog. Energy 50 (2024) 390–405. https://doi.org/10.1016/j.ijhydene.2023.07.126.
56. K. Ohira, Study of nucleate boiling heat transfer to slush hydrogen and slush nitrogen, Heat Transfer—Asian Res. 32 (2003) 13–28. https://doi.org/10.1002/htj.10068.
57. P.D. Harris, R. Barnes, The uses of helium and xenon in current clinical practice, Anaesthesia 63 (2008) 284–293. https://doi.org/10.1111/j.1365-2044.2007.05253.x.

 doi:10.20944/preprints202503.1980.v1

58. Y. Xie, K. Zhong, Investigation on the Performances of Vuilleumier Cycle Heat Pump Adopting Mixture Refrigerants, Entropy 19 (2017) 446. https://doi.org/10.3390/e19090446.
59. S.A. Usas, L. Ricardez-Sandoval, An optimal sustainable planning strategy for national carbon capture deployment: A review on the state of CO_2 capture in Canada, Can. J. Chem. Eng. (2024) cjce.25249. https://doi.org/10.1002/cjce.25249.
60. O.A. Marzouk, Subcritical and supercritical Rankine steam cycles, under elevated temperatures up to 900°C and absolute pressures up to 400 bara, Adv. Mech. Eng. 16 (2024) 1–18. https://doi.org/10.1177/16878132231221065.
61. O.A. Marzouk, Wind Speed Weibull Model Identification in Oman, and Computed Normalized Annual Energy Production (NAEP) From Wind Turbines Based on Data From Weather Stations, Eng. Rep. 7 (2025) e70089. https://doi.org/10.1002/eng2.70089.
62. O.A. Marzouk, Tilt sensitivity for a scalable one-hectare photovoltaic power plant composed of parallel racks in Muscat, Cogent Eng. 9 (2022) 2029243. https://doi.org/10.1080/23311916.2022.2029243.
63. Y. Shang, S. Sang, A.K. Tiwari, S. Khan, X. Zhao, Impacts of renewable energy on climate risk: A global perspective for energy transition in a climate adaptation framework, Appl. Energy 362 (2024) 122994. https://doi.org/10.1016/j.apenergy.2024.122994.
64. O.A. Marzouk, Energy Generation Intensity (EGI) of Solar Updraft Tower (SUT) Power Plants Relative to CSP Plants and PV Power Plants Using the New Energy Simulator "Aladdin," Energies 17 (2024) 405. https://doi.org/10.3390/en17020405.
65. N.S. Chipangamate, G.T. Nwaila, Assessment of challenges and strategies for driving energy transitions in emerging markets: A socio-technological systems perspective, Energy Geosci. 5 (2024) 100257. https://doi.org/10.1016/j.engeos.2023.100257.
66. M.A. Murmura, S. Cerbelli, M.C. Annesini, Transport-reaction-permeation regimes in catalytic membrane reactors for hydrogen production. The steam reforming of methane as a case study, Chem. Eng. Sci. 162 (2017) 88–103. https://doi.org/10.1016/j.ces.2016.12.046.
67. D.-K. Oh, K.-Y. Lee, J.-S. Park, Hydrogen Purification from Compact Palladium Membrane Module Using a Low Temperature Diffusion Bonding Technology, Membranes 10 (2020) 338. https://doi.org/10.3390/membranes10110338.
68. D. Berstad, P. Nekså, G.A. Gjøvåg, Low-temperature syngas separation and CO_2 capture for enhanced efficiency of IGCC power plants, Energy Procedia 4 (2011) 1260–1267. https://doi.org/10.1016/j.egypro.2011.01.182.
69. R.D. Brdar, R.M. Jones, GE IGCC Technology and Experience with Advanced Gas Turbines, General Electric (GE) Power Systems, 2021. https://www.ge.com/content/dam/gepower-new/global/en_US/downloads/gas-new-site/resources/reference/ger-4207-ge-igcc-technology-experience-advanced-gas-turbines.pdf (accessed May 6, 2022).
70. G. Krishnan, D. Steele, K. O'Brien, R. Callahan, K. Berchtold, J. Figueroa, Simulation of a Process to Capture CO_2 From IGCC Syngas Using a High Temperature PBI Membrane, Energy Procedia 1 (2009) 4079–4088. https://doi.org/10.1016/j.egypro.2009.02.215.
71. T. Wang, An overview of IGCC systems, in: Integr. Gasif. Comb. Cycle IGCC Technol., Elsevier, 2017: pp. 1–80. https://doi.org/10.1016/B978-0-08-100167-7.00001-9.
72. R. Pruschek, G. Oeljeklaus, R. Kloster, Enhancement of the efficiency of coal-fired power generation systems: final report, Institute for Process Engineering and Power Plant Technology, University of Stuttgart, Stuttgart, Germany, 1998. https://www.osti.gov/etdeweb/biblio/688545 (accessed February 27, 2025).
73. O.A. Marzouk, Condenser Pressure Influence on Ideal Steam Rankine Power Vapor Cycle using the Python Extension Package Cantera for Thermodynamics, Eng. Technol. Appl. Sci. Res. 14 (2024) 14069–14078. https://doi.org/10.48084/etasr.7277.
74. Mitsubishi Power, IGCC Integrated coal Gasification Combined Cycle Power Plants, Mitsubishi Power, a brand of Mitsubishi Heavy Industries, Ltd., 2021. https://power.mhi.com/catalogue/pdf/igcc.pdf (accessed May 6, 2022).

75. O.A. Marzouk, Chronologically-Ordered Quantitative Global Targets for the Energy-Emissions-Climate Nexus, from 2021 to 2050, in: 2022 Int. Conf. Environ. Sci. Green Energy ICESGE, IEEE [Institute of Electrical and Electronics Engineers], Virtual, 2022: pp. 1–6. https://doi.org/10.1109/ICESGE56040.2022.10180322.
76. Y. Zhao, D. Ying, Y. Liu, R. Wentao, Relative Stability Analysis Method of Systems Based on Goal Seek, in: 2021 3rd Int. Conf. Ind. Artif. Intell. IAI, 2021: pp. 1–5. https://doi.org/10.1109/IAI53119.2021.9619380.
77. H. Guerrero, Solver, Scenarios, and Goal Seek Tools, in: H. Guerrero (Ed.), Excel Data Anal. Model. Simul., Springer International Publishing, Cham, 2019: pp. 311–346. https://doi.org/10.1007/978-3-030-01279-3_9.
78. Y. Tian, C. Qin, Z. Yang, D. Hao, Numerical simulation study on the leakage and diffusion characteristics of high-pressure hydrogen gas in different spatial scenes, Int. J. Hydrog. Energy 50 (2024) 1335–1349. https://doi.org/10.1016/j.ijhydene.2023.10.253.
79. O.A. Marzouk, Contrasting the Cartesian and polar forms of the shedding-induced force vector in response to 12 subharmonic and superharmonic mechanical excitations, Fluid Dyn. Res. 42 (2010) 035507. https://doi.org/10.1088/0169-5983/42/3/035507.
80. K. Ghasemzadeh, T. Torabi, T. Yousefi Amiri, A. Fortunelli, A. Iulianelli, Parametric and sensitive analysis of Pd-Ag membrane reactor performance in biogas reforming to generate decarbonized hydrogen by Computational Fluid Dynamic-Response Surface Methodology, Fuel 365 (2024) 131205. https://doi.org/10.1016/j.fuel.2024.131205.
81. O.A. Marzouk, Characteristics of the Flow-Induced Vibration and Forces With 1- and 2-DOF Vibrations and Limiting Solid-to-Fluid Density Ratios, J. Vib. Acoust. 132 (2010) 041013. https://doi.org/10.1115/1.4001503.
82. A.H. Kassi, T.A. Al-Hattab, A CFD model of natural gas steam reforming in a catalytic membrane reactor: Effect of various operating parameters on the performance of CMR, Int. J. Hydrog. Energy 56 (2024) 780–796. https://doi.org/10.1016/j.ijhydene.2023.12.156.
83. O.A. Marzouk, A.H. Nayfeh, Characterization of the flow over a cylinder moving harmonically in the cross-flow direction, Int. J. Non-Linear Mech. 45 (2010) 821–833. https://doi.org/10.1016/j.ijnonlinmec.2010.06.004.
84. R. Zakeri, A. Fazeli, CFD modeling of hydrogen production from glycerol steam reforming in Tesla microchannel reactor, Fuel 357 (2024) 129646. https://doi.org/10.1016/j.fuel.2023.129646.
85. X. Li, Y. Zhao, Z. Liu, H. Chen, A new methodology for preliminary design of centrifugal impellers with prewhirl, Proc. Inst. Mech. Eng. Part J. Power Energy 234 (2020) 251–262. https://doi.org/10.1177/0957650919864193.
86. O.A. Marzouk, Evolutionary Computing Applied to Design Optimization, in: Vol. 2 27th Comput. Inf. Eng. Conf. Parts B, ASMEDC, Las Vegas, Nevada, USA, 2007: pp. 995–1003. https://doi.org/10.1115/DETC2007-35502.
87. Z. Zhang, Understanding and exploiting the nonlinear behavior of tuned liquid dampers (TLDs) for structural vibration control by means of a nonlinear reduced-order model (ROM), Eng. Struct. 251 (2022) 113524. https://doi.org/10.1016/j.engstruct.2021.113524.
88. O.A. Marzouk, Flow control using bifrequency motion, Theor. Comput. Fluid Dyn. 25 (2011) 381–405. https://doi.org/10.1007/s00162-010-0206-6.
89. O.A. Marzouk, A two-step computational aeroacoustics method applied to high-speed flows, Noise Control Eng. J. 56 (2008) 396. https://doi.org/10.3397/1.2978229.
90. J.Y. San, W.M. Worek, Z. Lavan, Entropy Generation in Convective Heat Transfer and Isothermal Convective Mass Transfer, J. Heat Transf. 109 (1987) 647–652. https://doi.org/10.1115/1.3248137.
91. [United States Department of Energy] DOE, Department of Energy Fundamentals Training Handbook, Thermodynamics, Heat Transfer, and Fluid Flow, Volume 2 of 3, United States Department of Energy (DOE), 1992. https://www.standards.doe.gov/standards-documents/1000/1012-bhdbk-1992-v2/@@images/file (accessed June 1, 2024).
92. Enerquip, What's the difference between parallel flow, counter flow and crossflow heat exchangers?, (2022). https://www.enerquip.com/whats-the-difference-between-parallel-flow-counter-flow-and-crossflow-heat-exchangers (accessed May 7, 2022).

 doi:10.20944/preprints202503.1980.v1

93. Thermex, Why counter flow heat exchangers are more efficient, (2022). http://www.thermex.co.uk/news/blog/605-why-counter-flow-heat-exchangers-are-more-efficient (accessed May 7, 2022).
94. R. Ben-Mansour, M.A. Haque, M.A. Habib, S. Paglieri, A. Harale, E.M.A. Mokheimer, Effect of temperature and heat flux boundary conditions on hydrogen production in membrane-integrated steam-methane reformer, Appl. Energy 346 (2023) 121407. https://doi.org/10.1016/j.apenergy.2023.121407.
95. G. Barbieri, Sweep Gas in a Membrane Reactor, in: E. Drioli, L. Giorno (Eds.), Encycl. Membr., Springer Berlin Heidelberg, Berlin, Heidelberg, 2015: pp. 1–2. https://doi.org/10.1007/978-3-642-40872-4_768-1.
96. Z. Li, J.M. Polfus, W. Xing, C. Denonville, M.-L. Fontaine, R. Bredesen, Factors Limiting the Apparent Hydrogen Flux in Asymmetric Tubular Cercer Membranes Based on $LaCO_{27}WCO_{3.5}MoCO_{1.5}O_{55.5-\delta}$ and $La_{0.87}Sr_{0.13}CrO$sub>3−δ</sub>, Membranes 9 (2019) 126. https://doi.org/10.3390/membranes9100126.
97. D. Xie, J. Yu, F. Wang, N. Zhang, W. Wang, H. Yu, F. Peng, A.-H.A. Park, Hydrogen permeability of Pd–Ag membrane modules with porous stainless steel substrates, Int. J. Hydrog. Energy 36 (2011) 1014–1026. https://doi.org/10.1016/j.ijhydene.2010.10.030.
98. R.Y. Chein, Y.C. Chen, J.N. Chung, Sweep gas flow effect on membrane reactor performance for hydrogen production from high-temperature water-gas shift reaction, J. Membr. Sci. 475 (2015) 193–203. https://doi.org/10.1016/j.memsci.2014.09.046.
99. U. Balachandran, S.E. Dorris, J.E. Emerson, T.H. Lee, Y. Lu, C.Y. Park, J.J. Picciolo, Hydrogen Separation Membranes, Argonne National Laboratory (ANL) of the United States Department of Energy, 2011. https://publications.anl.gov/anlpubs/2011/03/69523.pdf (accessed May 31, 2024).
100. N. Bidica, N. Ghimis, B. Monea, Experimental results of deuterium/hydrogen co-current permeation through Nickel membrane, in non-steady-state surface limited regime, Fusion Eng. Des. 194 (2023) 113718. https://doi.org/10.1016/j.fusengdes.2023.113718.
101. S. Escolástico, M. Ivanova, C. Solís, S. Roitsch, W.A. Meulenberg, J.M. Serra, Improvement of transport properties and hydrogen permeation of chemically-stable proton-conducting oxides based on the system $BaZr_{1-x-y}Y_xM_yO_{3-\delta}$, RSC Adv. 2 (2012) 4932. https://doi.org/10.1039/c2ra20214j.
102. G.R. Longhurst, A. Kratville, A Simple System for Measuring Permeation of Hydrogen Through Stainless Steel, Fusion Sci. Technol. 66 (2014) 385–393. https://doi.org/10.13182/FST14-801.
103. W.-H. Chen, C.-H. Lin, Y.-L. Lin, C.-W. Tsai, R.-Y. Chein, C.-T. Yu, Interfacial permeation phenomena of hydrogen purification and carbon dioxide separation in a non-isothermal palladium membrane tube, Chem. Eng. J. 305 (2016) 156–168. https://doi.org/10.1016/j.cej.2016.01.036.
104. P. Chiesa, M.C. Romano, T.G. Kreutz, Use of membranes in systems for electric energy and hydrogen production from fossil fuels, in: Handb. Membr. React., Elsevier, 2013: pp. 416–455. https://doi.org/10.1533/9780857097347.2.416.
105. P. Marín, Y. Patiño, F.V. Díez, S. Ordóñez, Modelling of hydrogen perm-selective membrane reactors for catalytic methane steam reforming, Int. J. Hydrog. Energy 37 (2012) 18433–18445. https://doi.org/10.1016/j.ijhydene.2012.08.147.
106. Y. Park, J. Cha, H.-T. Oh, T. Lee, S.H. Lee, M.G. Park, H. Jeong, Y. Kim, H. Sohn, S.W. Nam, J. Han, C.W. Yoon, Y.S. Jo, A catalytic composite membrane reactor system for hydrogen production from ammonia using steam as a sweep gas, J. Membr. Sci. 614 (2020) 118483. https://doi.org/10.1016/j.memsci.2020.118483.
107. A. Brunetti, A. Caravella, E. Drioli, G. Barbieri, CHAPTER 1. Membrane Reactors for Hydrogen Production, in: 2017: pp. 1–29. https://doi.org/10.1039/9781788010443-00001.
108. X. Li, A. Li, C.J. Lim, J.R. Grace, Hydrogen permeation through Pd-based composite membranes: Effects of porous substrate, diffusion barrier and sweep gas, J. Membr. Sci. 499 (2016) 143–155. https://doi.org/10.1016/j.memsci.2015.10.037.
109. X. Meng, Y. Shang, B. Meng, N. Yang, X. Tan, J. Sunarso, S. Liu, Bi-functional performances of $BaCe_{0.95}Tb_{0.05}O_{3-\delta}$-based hollow fiber membranes for power generation and hydrogen permeation, J. Eur. Ceram. Soc. 36 (2016) 4123–4129. https://doi.org/10.1016/j.jeurceramsoc.2016.06.041.
110. R.M. Roberts, T.S. Elleman, H.P. Iii, K. Verghese, Hydrogen Permeability of Sintered Aluminum Oxide, J. Am. Ceram. Soc. 62 (1979) 495–499. https://doi.org/10.1111/j.1151-2916.1979.tb19114.x.

 doi:10.20944/preprints202503.1980.v1

111. S. Escolástico, C. Solís, C. Kjølseth, J.M. Serra, Outstanding hydrogen permeation through CO_2-stable dual-phase ceramic membranes, Energy Env. Sci 7 (2014) 3736–3746. https://doi.org/10.1039/C4EE02066A.
112. X. Qi, Electrical conduction and hydrogen permeation through mixed proton–electron conducting strontium cerate membranes, Solid State Ion. 130 (2000) 149–156. https://doi.org/10.1016/S0167-2738(00)00281-2.
113. M. Sakbodin, E. Schulman, S.C. Oh, Y. Pan, E.D. Wachsman, D. Liu, Dual utilization of greenhouse gases to produce C_{2+} hydrocarbons and syngas in a hydrogen-permeable membrane reactor, J. Membr. Sci. 595 (2020) 117557. https://doi.org/10.1016/j.memsci.2019.117557.
114. J.B. Smith, K.I. Aasen, K. Wilhelmsen, D. Käka, T. Risdal, A. Berglund, A. Stenersen Østby, M. Budd, T. Bruun, B. Werswick, Recent development in the HMR pre-combustion gas power cycle, Energy Procedia 1 (2009) 343–351. https://doi.org/10.1016/j.egypro.2009.01.047.
115. X. Tan, X. Tan, N. Yang, B. Meng, K. Zhang, S. Liu, High performance BaCe0.8Y0.2O_{>>3−a} (BCY) hollow fibre membranes for hydrogen permeation, Ceram. Int. 40 (2014) 3131–3138. https://doi.org/10.1016/j.ceramint.2013.09.132.
116. D. Unruh, K. Pabst, G. Schaub, Fischer−Tropsch Synfuels from Biomass: Maximizing Carbon Efficiency and Hydrocarbon Yield, Energy Fuels 24 (2010) 2634–2641. https://doi.org/10.1021/ef9009185.
117. [Gas Technology Institute] GTI, Direct Hydrogen Production from Biomass Gasifier Using Hydrogen-Selective Membrane, Gas Technology Institute (GTI), In collaboration with Natural Resources Research Institute University of Minnesota at Duluth, 2007. https://www.xcelenergy.com/staticfiles/xe/Corporate/RDF-DirectHydrogenProduction-Report%5B1%5D.pdf (accessed May 31, 2024).
118. K. Kinouchi, M. Katoh, T. Horikawa, T. Yoshikawa, M. Wada, HYDROGEN PERMEABILITY OF PALLADIUM MEMBRANE FOR STEAM-REFORMING OF BIO-ETHANOL USING THE MEMBRANE REACTOR, Int. J. Mod. Phys. Conf. Ser. 06 (2012) 7–12. https://doi.org/10.1142/S2010194512002851.
119. P. Barnoon, Modeling of a high temperature heat exchanger to supply hydrogen required by fuel cells through reforming process, Energy Rep. 7 (2021) 5685–5699. https://doi.org/10.1016/j.egyr.2021.08.171.
120. P. Barnoon, D. Toghraie, B. Mehmandoust, M.A. Fazilati, S.A. Eftekhari, Comprehensive study on hydrogen production via propane steam reforming inside a reactor, Energy Rep. 7 (2021) 929–941. https://doi.org/10.1016/j.egyr.2021.02.001.
121. F. Fornarelli, L. Dambrosio, L. Terlizzi, S.M. Camporeale, Performance and cost multi objective optimisation of a shell-and-tube LHTES device for mid-temperature applications, J. Energy Storage 99 (2024) 113134. https://doi.org/10.1016/j.est.2024.113134.
122. M. Kirincic, A. Trp, K. Lenic, F. Torbarina, Numerical analysis of the influence of geometry parameters on charging and discharging performance of shell-and-tube latent thermal energy storage with longitudinal fins, Appl. Therm. Eng. 236 (2024) 121385. https://doi.org/10.1016/j.applthermaleng.2023.121385.
123. C. Li, Q. Li, R. Ge, Comparison of performance enhancement in a shell and tube based latent heat thermal energy storage device containing different structured fins, Renew. Energy 206 (2023) 994–1006. https://doi.org/10.1016/j.renene.2023.02.087.
124. O.A. Marzouk, Direct Numerical Simulations of the Flow Past a Cylinder Moving With Sinusoidal and Nonsinusoidal Profiles, J. Fluids Eng. 131 (2009) 121201. https://doi.org/10.1115/1.4000406.
125. M.R. Daneshparvar, R. Beigzadeh, Multi-objective optimization of helical baffles in the shell-and-tube heat exchanger by computational fluid dynamics and genetic algorithm, Energy Rep. 8 (2022) 11064–11077. https://doi.org/10.1016/j.egyr.2022.08.249.
126. O.A. Marzouk, One-way and two-way couplings of CFD and structural models and application to the wake-body interaction, Appl. Math. Model. 35 (2011) 1036–1053. https://doi.org/10.1016/j.apm.2010.07.049.
127. W.H. Saldanha, F.R.P. Arrieta, G.L. Soares, State-of-the-Art of Research on Optimization of Shell and Tube Heat Exchangers by Methods of Evolutionary Computation, Arch. Comput. Methods Eng. 28 (2021) 2761–2783. https://doi.org/10.1007/s11831-020-09476-4.
128. O.A. Marzouk, E.D. Huckaby, Simulation of a Swirling Gas-Particle Flow Using Different k-epsilon Models and Particle-Parcel Relationships, Eng. Lett. 18 (2010) 7. https://doi.org/10.5281/zenodo.14591654.

129. P. Li, L. Chen, S. Xia, L. Zhang, Entropy Generation Rate Minimization for Methanol Synthesis via a CO_2 Hydrogenation Reactor, Entropy 21 (2019) 174. https://doi.org/10.3390/e21020174.
130. P. Li, L. Chen, S. Xia, R. Kong, Y. Ge, Multi-objective optimal configurations of a membrane reactor for steam methane reforming, Energy Rep. 8 (2022) 527–538. https://doi.org/10.1016/j.egyr.2021.11.288.
131. P. Bichkar, O. Dandgaval, P. Dalvi, R. Godase, T. Dey, Study of Shell and Tube Heat Exchanger with the Effect of Types of Baffles, Procedia Manuf. 20 (2018) 195–200. https://doi.org/10.1016/j.promfg.2018.02.028.
132. E. Pal, I. Kumar, J.B. Joshi, N.K. Maheshwari, CFD simulations of shell-side flow in a shell-and-tube type heat exchanger with and without baffles, Chem. Eng. Sci. 143 (2016) 314–340. https://doi.org/10.1016/j.ces.2016.01.011.
133. U. Salahuddin, M. Bilal, H. Ejaz, A review of the advancements made in helical baffles used in shell and tube heat exchangers, Int. Commun. Heat Mass Transf. 67 (2015) 104–108. https://doi.org/10.1016/j.icheatmasstransfer.2015.07.005.
134. N. Jamsran, H. Park, J. Lee, S. Oh, C. Kim, Y. Lee, K. Kang, Influence of syngas composition on combustion and emissions in a homogeneous charge compression ignition engine, Fuel 306 (2021) 121774. https://doi.org/10.1016/j.fuel.2021.121774.
135. N. Kousheshi, M. Yari, A. Paykani, A. Saberi Mehr, G.F. de la Fuente, Effect of Syngas Composition on the Combustion and Emissions Characteristics of a Syngas/Diesel RCCI Engine, Energies 13 (2020) 212. https://doi.org/10.3390/en13010212.
136. A.M. Ribeiro, J.C. Santos, A.E. Rodrigues, PSA design for stoichiometric adjustment of bio-syngas for methanol production and co-capture of carbon dioxide, Chem. Eng. J. 163 (2010) 355–363. https://doi.org/10.1016/j.cej.2010.08.015.
137. A. Giuliano, C. Freda, E. Catizzone, Techno-Economic Assessment of Bio-Syngas Production for Methanol Synthesis: A Focus on the Water–Gas Shift and Carbon Capture Sections, Bioengineering 7 (2020) 70. https://doi.org/10.3390/bioengineering7030070.
138. [United States National Institute of Standards and Technology] NIST, NIST Chemistry WebBook - Hydrogen, (2021). https://webbook.nist.gov/cgi/cbook.cgi?Name=h2&Units=SI (accessed May 7, 2022).
139. [United States National Institute of Standards and Technology] NIST, NIST Chemistry WebBook - Carbon monoxide, (2021). https://webbook.nist.gov/cgi/cbook.cgi?Name=CO&Units=SI (accessed May 7, 2022).
140. [United States National Institute of Standards and Technology] NIST, NIST Chemistry WebBook - Carbon dioxide, (2021). https://webbook.nist.gov/cgi/cbook.cgi?ID=C124389&Units=SI (accessed May 7, 2022).
141. K.K. Kuo, Principles of Combustion, 2nd ed, John Wiley, Hoboken, NJ, 2005.
142. O.A. Marzouk, Estimated electric conductivities of thermal plasma for air-fuel combustion and oxy-fuel combustion with potassium or cesium seeding, Heliyon 10 (2024) e31697. https://doi.org/10.1016/j.heliyon.2024.e31697.
143. T. Poinsot, D. Veynante, Theoretical and Numerical Combustion, 2nd ed, Edwards, Philadelphia, 2005.
144. [International Union of Pure and Applied Chemistry] IUPAC, IUPAC Compendium of Chemical Terminology, 3rd ed. Online version 3.0.1, (2019). https://doi.org/10.1351/goldbook.S06036 (accessed June 1, 2024).
145. [United States National Institute of Standards and Technology] NIST, CODATA [Committee on Data for Science and Technology] Value: molar gas constant, (2018). https://physics.nist.gov/cgi-bin/cuu/Value?r (accessed May 7, 2022).
146. [United States National Institute of Standards and Technology] NIST, NIST Chemistry WebBook - Nitrogen, (2021). https://webbook.nist.gov/cgi/cbook.cgi?Name=n2 (accessed May 7, 2022).
147. M. Utamura, K. Nikitin, Y. Kato, A generalised mean temperature difference method for thermal design of heat exchangers, Int. J. Nucl. Energy Sci. Technol. 4 (2008) 11. https://doi.org/10.1504/IJNEST.2008.017545.
148. J.H. Lienhard IV, J.H. Lienhard V., A Heat Transfer Textbook (fifth edition), 5th ed., Phlogiston Press, 2019.
149. O.A. Marzouk, Energy Generation Intensity (EGI) for Parabolic Dish/Engine Concentrated Solar Power in Muscat, Sultanate of Oman, IOP Conf. Ser. Earth Environ. Sci. 1008 (2022) 012013. https://doi.org/10.1088/1755-1315/1008/1/012013.
150. S. Bandyopadhyay, All forms of energy are equal, but some forms of energy are more equal than others, Clean Technol. Environ. Policy 23 (2021) 2775–2776. https://doi.org/10.1007/s10098-021-02228-3.

151. A. Demirbas, Balubaid, M. A., Basahel, A. M., Ahmad, W., M.H. and Sheikh, Octane Rating of Gasoline and Octane Booster Additives, Pet. Sci. Technol. 33 (2015) 1190–1197. https://doi.org/10.1080/10916466.2015.1050506.
152. J. Kubesh, S.R. King, W.E. Liss, Effect of Gas Composition on Octane Number of Natural Gas Fuels, in: San Francisco, California, USA, 1992: p. 922359. https://doi.org/10.4271/922359.
153. G. Leonzio, Methanol Synthesis: Optimal Solution for a Better Efficiency of the Process, Processes 6 (2018) 20. https://doi.org/10.3390/pr6030020.
154. E.C.D. Tan, M. Talmadge, A. Dutta, J. Hensley, J. Schaidle, M. Biddy, D. Humbird, L.J. Snowden-Swan, J. Ross, D. Sexton, R. Yap, J. Lukas, Process Design and Economics for the Conversion of Lignocellulosic Biomass to Hydrocarbons via Indirect Liquefaction Thermochemical Research Pathway to High-Octane Gasoline Blendstock Through Methanol/Dimethyl Ether Intermediates, National Renewable Energy Laboratory (NREL) and Pacific Northwest National Laboratory (PNNL) of the United States Department of Energy, 2015. https://www.nrel.gov/docs/fy15osti/62402.pdf (accessed June 1, 2024).
155. A. Vita, C. Italiano, Fuel and hydrogen related problems for conventional steam reforming of natural gas, in: Curr. Trends Future Dev. Bio- Membr., Elsevier, 2020: pp. 71–89. https://doi.org/10.1016/B978-0-12-816778-6.00004-7.
156. O.A. Marzouk, Lookup Tables for Power Generation Performance of Photovoltaic Systems Covering 40 Geographic Locations (Wilayats) in the Sultanate of Oman, with and without Solar Tracking, and General Perspectives about Solar Irradiation, Sustainability 13 (2021) 13209. https://doi.org/10.3390/su132313209.
157. C. Heumann, M. Schomaker, Shalabh, Introduction to Statistics and Data Analysis: with exercises, solutions and applications in r, 2nd ed., Springer Cham, 2023. https://link.springer.com/book/10.1007/978-3-031-11833-3.
158. O.A. Marzouk, E.D. Huckaby, A Comparative Study of Eight Finite-Rate Chemistry Kinetics for CO/H_2 Combustion, Eng. Appl. Comput. Fluid Mech. 4 (2010) 331–356. https://doi.org/10.1080/19942060.2010.11015322.
159. S. Wang, X. Lei, B. Xu, W. Jiang, L. Kong, B. Yang, Y. Tian, Y. Liu, Vacuum evaporation and condensation thermodynamics and evaporation kinetics of pure silver, Mater. 4 (2024) 100189. https://doi.org/10.1016/j.nxmate.2024.100189.
160. O.A. Marzouk, W.A.M.H.R. Jul, A.M.K. Al Jabri, H.A.M.A. Al-ghaithi, Construction of a Small-Scale Vacuum Generation System and Using It as an Educational Device to Demonstrate Features of the Vacuum, Int. J. Contemp. Educ. 1 (2018) 1–11. https://doi.org/10.48550/arXiv.2502.04340.
161. Alicat Scientific, Alicat flow controller - MC · MCW · MCR · MCV, Alicat Scientific, Inc. (a Halma company), Tucson, Arizona, USA, 2020. https://documents.alicat.com/manuals/Gas_Flow_Controller_Manual.pdf (accessed June 1, 2024).
162. N. Arshi, J. Lu, Y.K. Joo, C.G. Lee, J.H. Yoon, F. Ahmed, Study on structural, morphological and electrical properties of sputtered titanium nitride films under different argon gas flow, Mater. Chem. Phys. 134 (2012) 839–844. https://doi.org/10.1016/j.matchemphys.2012.03.078.
163. V. Ralchenko, I. Sychov, I. Vlasov, A. Vlasov, V. Konov, A. Khomich, S. Voronina, Quality of diamond wafers grown by microwave plasma CVD: effects of gas flow rate, Diam. Relat. Mater. 8 (1999) 189–193. https://doi.org/10.1016/S0925-9635(98)00427-0.
164. C. Rombouts, M. Bair, J. Barbe, J.D. Wright, R. Kramer, Z. Krajicek, A Comparison of Primary Gas Flow Standards Spanning the Range from 10 sccm N_2 to 10 slm N_2, NCSLI Meas. 9 (2014) 46–54. https://doi.org/10.1080/19315775.2014.11721705.
165. A. Ahmadi, N.L. Hadipour, M. Kamfiroozi, Z. Bagheri, Theoretical study of aluminum nitride nanotubes for chemical sensing of formaldehyde, Sens. Actuators B Chem. 161 (2012) 1025–1029. https://doi.org/10.1016/j.snb.2011.12.001.
166. R.F. Berg, T. Gooding, R.E. Vest, Constant pressure primary flow standard for gas flows from 0.01cm^3/min to 100cm^3/min (0.007–74μmol/s), Flow Meas. Instrum. 35 (2014) 84–91. https://doi.org/10.1016/j.flowmeasinst.2013.12.002.

167. R. Fillet, V. Nicolas, A. Celzard, V. Fierro, Solar evaporation performance of 3D-printed concave structures filled with activated carbon under low convective flow, Chem. Eng. J. 457 (2023) 141168. https://doi.org/10.1016/j.cej.2022.141168.
168. J. Jing, L. Yang, X. Tang, P. He, K. Tang, Numerical Simulation of Multiphase Flow Erosion in the Gas Well Relief Line Elbow under Supercritical Conditions, J. Pipeline Syst. Eng. Pract. 14 (2023) 04023031. https://doi.org/10.1061/JPSEA2.PSENG-1457.
169. M. Shahid, B. Chambers, S. Sankarasubramanian, Methane and oxygen from energy-efficient, low temperature in situ resource utilization enables missions to Mars, AIChE J. 69 (2023) e18010. https://doi.org/10.1002/aic.18010.
170. Y. Cao, W. Liang, C.K. Law, Real Gas Effects in High-Pressure Ignition of *n* -Dodecane/Air Mixtures, J. Phys. Chem. A 128 (2024) 3604–3612. https://doi.org/10.1021/acs.jpca.3c08395.
171. H. Ding, Y. Zhang, Y. Dong, C. Wen, Y. Yang, High-pressure supersonic carbon dioxide (CO_2) separation benefiting carbon capture, utilisation and storage (CCUS) technology, Appl. Energy 339 (2023) 120975. https://doi.org/10.1016/j.apenergy.2023.120975.
172. V. Gaganis, D. Homouz, M. Maalouf, N. Khoury, K. Polychronopoulou, An Efficient Method to Predict Compressibility Factor of Natural Gas Streams, Energies 12 (2019) 2577. https://doi.org/10.3390/en12132577.
173. M.A. Kartal, G. Atakök, S. Ersoy, Cooling and Multiphase Analysis of Heated Environmentally Friendly R152A (C2H4F2) Fluid Coming from the Production Process According to Nist Indicators, Appl. Sci. 14 (2024) 4143. https://doi.org/10.3390/app14104143.
174. M. Manfredi, G. Persico, A. Spinelli, P. Gaetani, V. Dossena, Design and commissioning of experiments for supersonic ORC nozzles in linear cascade configuration, Appl. Therm. Eng. 224 (2023) 119996. https://doi.org/10.1016/j.applthermaleng.2023.119996.
175. L.M. Ruiz Maraggi, L.G. Moscardelli, Modeling hydrogen storage capacities, injection and withdrawal cycles in salt caverns: Introducing the GeoH$_2$ salt storage and cycling app, Int. J. Hydrog. Energy 48 (2023) 26921–26936. https://doi.org/10.1016/j.ijhydene.2023.03.293.
176. N. Srinivasan, H. Zhang, S. Yang, VLE-Based Phase Field Method to Simulate High-Pressure Diffuse Interface with Phase Change, in: AIAA SCITECH 2024 Forum, American Institute of Aeronautics and Astronautics, Orlando, FL, 2024. https://doi.org/10.2514/6.2024-1635.
177. M. Mahmoud, Development of a New Correlation of Gas Compressibility Factor (Z-Factor) for High Pressure Gas Reservoirs, J. Energy Resour. Technol. 136 (2013). https://doi.org/10.1115/1.4025019.
178. O.A. Marzouk, The Sod gasdynamics problem as a tool for benchmarking face flux construction in the finite volume method, Sci. Afr. 10 (2020) e00573. https://doi.org/10.1016/j.sciaf.2020.e00573.
179. J.L. Bischoff, R.J. Rosenbauer, K.S. Pitzer, The system NaCl-H$_2$O: Relations of vapor-liquid near the critical temperature of water and of vapor-liquid-halite from 300° to 500°C, Geochim. Cosmochim. Acta 50 (1986) 1437–1444. https://doi.org/10.1016/0016-7037(86)90317-0.
180. J.-P. Dauchot, J.-P. Dath, Oxidation of carbon monoxide on thin film catalysts: Characterization by a critical temperature measurement, J. Catal. 86 (1984) 373–383. https://doi.org/10.1016/0021-9517(84)90382-8.
181. G. Guo, F. Wang, G.-Q. Liu, S.-J. Luo, R.-B. Guo, Calculation on the phase equilibrium and critical temperature of CH_4/CO_2, Process Saf. Environ. Prot. 113 (2018) 369–377. https://doi.org/10.1016/j.psep.2017.11.007.
182. S.E. Ingebritsen, D.O. Hayba, Fluid flow and heat transport near the critical point of H $_2$ O, Geophys. Res. Lett. 21 (1994) 2199–2202. https://doi.org/10.1029/94GL02002.
183. V.A. Karnaukhov, H. Oeschler, S.P. Avdeyev, E.V. Duginova, V.K. Rodionov, A. Budzanowski, W. Karcz, O.V. Bochkarev, E.A. Kuzmin, L.V. Chulkov, E. Norbeck, A.S. Botvina, Critical temperature for the nuclear liquid-gas phase transition, Phys. Rev. C 67 (2003) 011601. https://doi.org/10.1103/PhysRevC.67.011601.
184. J. Kestin, Ö. Korfali, J.V. Sengers, Density expansion of the viscosity of carbon dioxide near the critical temperature, Phys. Stat. Mech. Its Appl. 100 (1980) 335–348. https://doi.org/10.1016/0378-4371(80)90124-7.
185. I. Dincer, C. Zamfirescu, 1.5 Thermodynamic Aspects of Energy, in: Compr. Energy Syst., Elsevier, 2018: pp. 153–211. https://doi.org/10.1016/B978-0-12-809597-3.00105-X.
186. D. Tiab, E.C. Donaldson, Introduction to Petroleum Geology, in: Petrophysics, Elsevier, 2016: pp. 23–66. https://doi.org/10.1016/B978-0-12-803188-9.00002-4.

 doi:10.20944/preprints202503.1980.v1

187. U. Sankar Behera, S. Kumar Prasad, H.-S. Byun, Experimental validation on the phase separation for the 2-(Diisopropylamino)ethyl methacrylate and Poly [2-(diisopropylamino)ethyl methacrylate] in supercritical CO_2, J. Mol. Liq. 393 (2024) 123553. https://doi.org/10.1016/j.molliq.2023.123553.
188. Z. Shang, Y. Yang, L. Zhang, H. Sun, J. Zhong, K. Zhang, J. Yao, Hydrogen adsorption and diffusion behavior in kaolinite slit for underground hydrogen storage: A hybrid GCMC-MD simulation study, Chem. Eng. J. 487 (2024) 150517. https://doi.org/10.1016/j.cej.2024.150517.
189. Y. Shen, C. Qiu, D. Liu, X. Tao, A. Wan, Z. Zhang, Z. Gan, Experimental study on a closed-cycle Joule-Thomson cryocooler working at liquid hydrogen temperature, Appl. Therm. Eng. 234 (2023) 121291. https://doi.org/10.1016/j.applthermaleng.2023.121291.
190. C. Wei-yu, L. Sun, J. Zhou, X. Li, L. Huang, G. Xia, X. Meng, K. Wang, Toward Predicting Interfacial Tension of Impure and Pure CO $_2$ -Brine Systems Using Robust Correlative Approaches, ACS Omega (2024) acsomega.3c07956. https://doi.org/10.1021/acsomega.3c07956.
191. Y. Xie, H. Dong, S. Zhang, X. Lu, X. Ji, Solubilities of CO_2, CH_4, H_2, CO and N_2 in choline chloride/urea, Green Energy Environ. 1 (2016) 195–200. https://doi.org/10.1016/j.gee.2016.09.001.
192. S. Mihara, H. Sagara, Y. Arai, S. Saito, The compressibility factors of hydrogen-methane, hydrogen-ethane and hydrogen-propane gaseous mixtures., J. Chem. Eng. Jpn. 10 (1977) 395–399. https://doi.org/10.1252/jcej.10.395.
193. O.A. Marzouk, Thermo Physical Chemical Properties of Fluids Using the Free NIST Chemistry WebBook Database, Fluid Mech. Res. Int. J. 1 (2017). https://doi.org/10.15406/fmrij.2017.01.00003.
194. [Pacific Northwest National Laboratory of the United States Department of Energy] PNNL, H2 Tools - Hydrogen Compressibility at different temperatures and pressures, (2022). https://h2tools.org/hyarc/hydrogen-data/hydrogen-compressibility-different-temperatures-and-pressures (accessed September 20, 2022).
195. [Center for Chemical Process Safety of the American Institute of Chemical Engineers] CCPS, Plug Flow Reactor (PFR), (2022). https://www.aiche.org/ccps/resources/glossary/process-safety-glossary/plug-flow-reactor-pfr (accessed September 20, 2022).
196. D. Ming, D. Glasser, D. Hildebrandt, B. Glasser, M. Metzer, Attainable region theory: an introduction to choosing an optimal reactor, Wiley, Hoboken, New Jersey, 2016.
197. D. Rosa, P. Goes, J. Manzi, Steady-State Plug Flow Reactor Analysis by means of Minimum Entropy, in: Comput. Aided Chem. Eng., Elsevier, 2017: pp. 1165–1170. https://doi.org/10.1016/B978-0-444-63965-3.50196-3.
198. R. Curtis, C. Nguyen, S. Lower, 2.3: First-Order Reactions, (2021). https://chem.libretexts.org/Bookshelves/Physical_and_Theoretical_Chemistry_Textbook_Maps/Supplemental_Modules_(Physical_and_Theoretical_Chemistry)/Kinetics/02%3A_Reaction_Rates/2.03%3A_First-Order_Reactions (accessed September 20, 2022).
199. K. Phuakpunk, B. Chalermsinsuwan, S. Assabumrungrat, Comparison of chemical reaction kinetic models for corn cob pyrolysis, Energy Rep. 6 (2020) 168–178. https://doi.org/10.1016/j.egyr.2020.08.041.
200. O.A. Marzouk, A.H. Nayfeh, New Wake Models With Capability of Capturing Nonlinear Physics, in: ASME 2008 27th Int. Conf. Offshore Mech. Arct. Eng. OMAE 2008, ASME [American Society of Mechanical Engineers], Estoril, Portugal, 2009: pp. 901–912. https://doi.org/10.1115/OMAE2008-57714.
201. O.A. Marzouk, A.H. Nayfeh, A Study of the Forces on an Oscillating Cylinder, in: ASME 2007 26th Int. Conf. Offshore Mech. Arct. Eng. OMAE 2007, ASME [American Society of Mechanical Engineers], San Diego, California, USA, 2009: pp. 741–752. https://doi.org/10.1115/OMAE2007-29163.
202. [American Institute of Chemical Engineers] AIChE, Plug Flow Reactor (PFR), (2022). https://www.aiche.org/ccps/resources/glossary/process-safety-glossary/plug-flow-reactor-pfr (accessed May 9, 2022).
203. M.E. Tuckerman, Lecture 25: Plug flow reactors and comparison to continuously stirred tank reactors, (2020). https://chem.libretexts.org/Courses/New_York_University/CHEM-UA_652%3A_Thermodynamics_and_Kinetics/Lecture_25%3A_Plug_flow_reactors_and_comparison_to_continuously_stirred_tank_reactors (accessed May 9, 2022).

204. O.A. Marzouk, Coupled differential-algebraic equations framework for modeling six-degree-of-freedom flight dynamics of asymmetric fixed-wing aircraft, Int. J. Appl. Adv. Sci. 12 (2025) 30–51. https://doi.org/10.21833/ijaas.2025.01.004.
205. C. Brencio, F.W.A. Fontein, J.A. Medrano, L. Di Felice, A. Arratibel, F. Gallucci, Pd-based membranes performance under hydrocarbon exposure for propane dehydrogenation processes: Experimental and modeling, Int. J. Hydrog. Energy 47 (2022) 11369–11384. https://doi.org/10.1016/j.ijhydene.2021.09.252.
206. M. Campo, A. Tanaka, A. Mendes, J.M. Sousa, Characterization of membranes for energy and environmental applications, in: Adv. Membr. Sci. Technol. Sustain. Energy Environ. Appl., Elsevier, 2011: pp. 56–89. https://doi.org/10.1533/9780857093790.1.56.
207. A. Caravella, S. Hara, E. Drioli, G. Barbieri, Sieverts law pressure exponent for hydrogen permeation through Pd-based membranes: Coupled influence of non-ideal diffusion and multicomponent external mass transfer, Int. J. Hydrog. Energy 38 (2013) 16229–16244. https://doi.org/10.1016/j.ijhydene.2013.09.102.
208. D. Olander, K. Konashi, M. Yamawaki, Uranium–Zirconium Hydride Fuel, in: Compr. Nucl. Mater., Elsevier, 2012: pp. 313–357. https://doi.org/10.1016/B978-0-08-056033-5.00061-6.
209. A. Suzuki, H. Yukawa, A Review for Consistent Analysis of Hydrogen Permeability through Dense Metallic Membranes, Membranes 10 (2020) 120. https://doi.org/10.3390/membranes10060120.
210. S.A. Koffler, J.B. Hudson, G.S. Ansell, Hydrogen permeation through alpha-palladium, Trans. Metall. Soc. Am. Inst. Min. Metall. Pet. Eng. 245 (1969) 1735–1740.
211. B.D. Morreale, M.V. Ciocco, R.M. Enick, B.I. Morsi, B.H. Howard, A.V. Cugini, K.S. Rothenberger, The permeability of hydrogen in bulk palladium at elevated temperatures and pressures, J. Membr. Sci. 212 (2003) 87–97. https://doi.org/10.1016/S0376-7388(02)00456-8.
212. M. Yuan, K. Lee, D.G. Van Campen, S. Liguori, M.F. Toney, J. Wilcox, Hydrogen Purification in Palladium-Based Membranes: An Operando X-ray Diffraction Study, Ind. Eng. Chem. Res. 58 (2019) 926–934. https://doi.org/10.1021/acs.iecr.8b05017.
213. O.A. Marzouk, Performance analysis of shell-and-tube dehydrogenation module, Int. J. Energy Res. 41 (2017) 604–610. https://doi.org/10.1002/er.3637.
214. M. Nordio, S.A. Wassie, M. Van Sint Annaland, D.A. Pacheco Tanaka, J.L. Viviente Sole, F. Gallucci, Techno-economic evaluation on a hybrid technology for low hydrogen concentration separation and purification from natural gas grid, Int. J. Hydrog. Energy 46 (2021) 23417–23435. https://doi.org/10.1016/j.ijhydene.2020.05.009.
215. O.A. Marzouk, Levelized cost of green hydrogen (LCOH) in the Sultanate of Oman using H2A-Lite with polymer electrolyte membrane (PEM) electrolyzers powered by solar photovoltaic (PV) electricity, E3S Web Conf. 469 (2023) 00101. https://doi.org/10.1051/e3sconf/202346900101.
216. Microsoft Corporation, Use Goal Seek to find the result you want by adjusting an input value, (2022). https://support.microsoft.com/en-us/office/use-goal-seek-to-find-the-result-you-want-by-adjusting-an-input-value-320cb99e-f4a4-417f-b1c3-4f369d6e66c7 (accessed May 11, 2022).